On the properties of Alfvénic switchbacks in the expanding solar wind: the influence of the Parker spiral

Jonathan Squire,[1] Zade Johnston,[1] Alfred Mallet,[2] and Romain Meyrand[1]

[1]*Physics Department, University of Otago, Dunedin 9010, New Zealand*
[2]*Space Sciences Laboratory, University of California, Berkeley, CA 94720, USA*
(*jonathan.squire@otago.ac.nz)

(Dated: May 20, 2022)

Switchbacks — rapid, large deflections of the solar wind's magnetic field — have generated significant interest as possible signatures of the key mechanisms that heat the corona and accelerate the solar wind. In this context, an important task for theories of switchback formation and evolution is to understand their observable distinguishing features, allowing them to be assessed in detail using spacecraft data. Here, we work towards this goal by studying the influence of the Parker spiral on the evolution of Alfvénic switchbacks in an expanding plasma. Using simple analytic arguments based on the physics of one-dimensional spherically polarized (constant-field-magnitude) Alfvén waves, we find that, by controlling the wave's obliquity, a Parker spiral strongly impacts switchback properties. Surprisingly, the Parker spiral can significantly enhance switchback formation, despite normalized wave amplitudes growing more slowly in its presence. In addition, switchbacks become strongly asymmetric: large switchbacks preferentially involve magnetic-field rotations in the plane of the Parker spiral (tangential deflections) rather than perpendicular (normal) rotations, and such deflections are strongly "tangentially skewed," meaning switchbacks always involve field rotations in the same direction (towards the positive-radial direction for an outwards mean field). In a companion paper, we show that these properties also occur in turbulent 3-D fields with switchbacks, with various caveats. These results demonstrate that substantial care is needed in assuming that specific features of switchbacks can be used to infer properties of the low corona; asymmetries and nontrivial correlations can develop as switchbacks propagate due to the interplay between expansion and spherically polarized, divergence-free magnetic fields.

I. INTRODUCTION

Early observations of switchbacks by Parker Solar Probe (PSP) provided a stark demonstration of the dynamic nature of the near-Sun solar wind [1]. These strong and sudden reversals of the background magnetic field, which are known from electron measurements to have the topology of local folds in field lines (as opposed to global polarity reversals [2]), contain significant energy content compared to the background plasma. This suggests they play a role in — or are least a helpful diagnostic of — the key processes that heat and accelerate the solar wind [3]. As such, a range of different explanations have been put forth for their origin, each relating in some way to fundamental low-coronal or solar-wind physics with the switchbacks emerging as an observable consequence. These explanations include models relating to interchange reconnection near the solar surface [4–7], low-coronal jets or other motions [8, 9], field-line folding due to asymmetries from interchange reconnection [10], instabilities between different wind streams [11], or the growth of Alfvénic fluctuations due to plasma expansion [12–14]. Given these widely differing ideas, each of which provide different predictions for switchback properties and occurrence rate, a clear path forward to bettering our understanding of the solar wind presents itself: quantify various (hopefully) unique and observationally testable predictions for each model, then compare these to observations.

In this paper, we continue this process of better understanding model predictions for the scenario where switchbacks form due to the growth of Alfvénic fluctuations. This scenario, which is most naturally associated with wave-driven solar-wind acceleration theories [15, 16], is in some sense the simplest of all those mentioned above — it requires Alfvén waves of some form to be released into the low corona [17]; in growing to normalized amplitudes $\gtrsim 1$ due to expansion they create switchbacks. Importantly, the scenario does not assume anything in particular about the process that creates the Alfvénic fluctuations in the first place, but concerns only the role of expansion and the assertion that (because they are Alfvénic) they should be "spherically polarized," *viz.,* have a constant magnetic field strength (as is observed [18]). Thus, its predictions relate exclusively to how fluctuations grow and change shape as they propagate. Accordingly, if a particular correlation, structure, or feature arises as a basic prediction of the scenario, this would arise naturally from almost any mechanism that generates Alfvénic fluctuations at low altitudes. While this certainly does not eliminate the possibility that the original fluctuations result from an interesting mechanism (e.g., interchange reconnection), it does undermine the credibility of using switchbacks as evidence for the importance of this mechanism. Several examples of this mindset have already been discussed in theory of Ref. 14 (hereafter M+21), which argues, for example, that Alfvénic switchbacks are preferentially elongated along the background magnetic field as a simple consequence of being divergence free, as well as predicting various non-trivial compressive correlations that result from expansion.

In this paper, we consider how the Parker spiral — the azimuthal rotation of the mean field with increasing heliocentric radius [19] — influences the evolution of Alfvénic switchbacks in an expanding plasma. Our core results are based on the idealized physics governing the evolution of large-amplitude, one-dimensional waves. We predict a number of surprising features and asymmetries that arise because

of the Parker spiral's effect on the wave's obliquity. Despite their idealized nature, however, these results seem to be well confirmed by our companion paper Ref. 20 (hereafter J+22), which is designed to be considered in conjunction with this work. J+22 shares the same overarching goal of honing the predictions of the Alfvénic switchback model, but uses realistic 3-D expanding magnetohydrodynamic (MHD) simulations that capture the full complexity of 3-D structures, turbulence, and compressibility. Thus, despite the obvious limitations of treating 1-D waves (some of which are quite severe), the approach seems to yield useful dividends in straightforwardly understanding a number of seemingly perplexing properties of switchbacks in 3-D simulations. Our hope — backed by some preliminary evidence — is that such conclusions apply also to the real solar wind.

The main result of this work (likewise, a key result of J+22), is that the Parker spiral causes switchbacks to become pronouncedly asymmetric in a number of ways. Defining the radial (R), tangential (T), normal (N) directions in the usual way — the Parker spiral lies in the radial-tangential (R-T) plane with a component in the +T direction, while normal is perpendicular to the R-T plane (see Fig. 1) — we show, among other results, that: (i) switchbacks preferentially involve field deflections in the R-T plane, as opposed to the normal direction (ii) switchbacks prevalence and intensity is enhanced by the Parker spiral, and (iii) field deflections become strongly "tangentially skewed," meaning they always deflect towards the positive radial direction in an outwards mean field, as opposed to the opposite direction (more generally, they deflect towards the mean field's radial component). A corollary of point (iii) is that the most common magnetic-field direction (its mode) can be very different to its mean, because its probability density function is highly skewed. Per our discussion above, this implies that any fluctuation directional asymmetries in observed switchbacks do not necessarily signify that the original source of the switchbacks is asymmetric; rather, asymmetries (of our predicted form) arise organically due to plasma expansion as fluctuations propagate outwards.

The remainder of the paper is organized as follows. Section II provides the necessary background to our calculations, introducing key concepts such as the definition of a nonlinear Alfvén wave, and how the divergence-free and constant-magnetic-field-strength constraints determine its associated fluctuations parallel to the mean field. This section effectively summarizes some key results of M+21, which forms the basis for our work. Section III presents results related to how the size of the parallel field perturbation, which is loosely interpreted as the switchback prevalence, evolves in 1-D waves as they grow and decay due to expansion. We will see that the Parker spiral has a strong influence because of its effect on the evolution of the wave's obliquity. Section IV then considers the magnetic-field structure of switchbacks that evolve as discussed in § III, illustrating their tangential skewness and providing a simple proof for why this occurs in 1-D. Section V is then concerned with the thorny question of how our 1-D results can apply to fully 3-D fields, including the effects of 3-D structure, turbulence and parametric decay, with reference to many of the results from J+22. We see that the results cannot be universally applicable but can likely be reasonably applied to certain regimes, so long as various important caveats are kept in mind. We conclude in § VI.

Three appendices present tangential results. Appendix A provides a different, 3-D, argument for the main results of § III based on integrating over a spectrum of waves that has been influenced by plasma expansion. Appendix B provides a cursory comparison of idealized wave results based on M+21 to two-dimensional MHD simulations with expansion, showing mostly good agreement (and allowing better understanding of a case where the method of M+21 fails). Appendix C demonstrates that, independently of the mean-field direction, wave amplitudes scale with expansion in the same way.

II. NONLINEAR ALFVÉN WAVES AND THE INFLUENCE OF EXPANSION

In this section, we discuss and derive some key properties of large-amplitude Alfvén waves, which will form the basis for our analysis of how such waves evolve in an expanding plasma with a Parker spiral. Our focus is on how such waves create switchbacks, *viz.,* under what conditions they can reverse the mean field. Our notation used below is as follows: P, ρ, $\boldsymbol{u}$ and $\boldsymbol{B}$ are the plasma's thermal pressure, density, flow velocity, and magnetic field. Where appropriate, we will denote spatial averaging with a bar (e.g., $\overline{\boldsymbol{B}}$) and fluctuating quantities (i.e., the remainder) with a δ (e.g., $\delta\boldsymbol{B}$), using periodic boundary conditions. In order to clarify notation, we will almost exclusively reference the mean field through the Alfvén speed, $\boldsymbol{v}_\mathrm{A} \equiv \overline{\boldsymbol{B}}/\sqrt{4\pi\overline{\rho}}$, and reference magnetic field fluctuations (i.e. the waves) in velocity units $\boldsymbol{b} \equiv \delta\boldsymbol{B}/\sqrt{4\pi\rho}$. We will work in the comoving frame in which $\delta\boldsymbol{u} = \boldsymbol{u}$ ($\overline{\boldsymbol{u}} = 0$). The magnetic field strength is $B = |\boldsymbol{B}|$ or $v_\mathrm{A} = |\boldsymbol{v}_\mathrm{A}|$, and we will use $\hat{}$ to denote unit vectors (e.g., $\hat{\boldsymbol{v}}_\mathrm{A} = \boldsymbol{v}_\mathrm{A}/v_\mathrm{A}$). In the discussion of waves, $\boldsymbol{p}$ denotes the wavevector, which makes an angle ϑ to $\boldsymbol{v}_\mathrm{A}$ ($\cos\vartheta = \hat{\boldsymbol{p}}\cdot\hat{\boldsymbol{v}}_\mathrm{A}$). In the discussion of expansion, a will denote the plasma's expansion factor (starting from some reference position with $a = 1$) and the coordinate system is Cartesian $\boldsymbol{x} = (x, y, z)$, with x the radial direction (that of the mean flow in the solar wind), y the tangential direction, and z the normal direction.

The basis for all of our discussion is the realisation [21] that

$$P = \text{const.}, \quad \rho = \text{const.}, \quad B^2 = \text{const.}, \quad \delta\boldsymbol{u} = \pm\boldsymbol{b} \tag{1}$$

is a nonlinear solution to the compressible MHD equations, which propagates along the mean field at the Alfvén speed. More generally, the solution (1) is valid even for the Kinetic MHD equations that describe large-scale collisionless dynamics [22, 23], if P is replaced with separate constraints on the perpendicular and parallel pressure and $\boldsymbol{v}_\mathrm{A}$ is modified to account for any mean pressure anisotropy (in fact, it is valid under even more general conditions than this; see Ref. 24). Here $\boldsymbol{b}$ can be of arbitrary amplitude compared to $\boldsymbol{v}_\mathrm{A}$, but $B = |\overline{\boldsymbol{B}} + \delta\boldsymbol{B}|$ (or $|\boldsymbol{v}_\mathrm{A} + \boldsymbol{b}| = \text{const.}$) must include both the mean-field and fluctuation contributions. Such solutions are the natural generalization of Alfvénic fluctuations to nonlin-

ear amplitudes [21] and are often referred to as spherically polarized waves.

A. One-dimensional nonlinear Alfvén waves and field reversals

Although Eq. (1) is valid for general three-dimensional $\boldsymbol{b}$, we now specialize to 1-D solutions that vary only along the direction $\hat{\boldsymbol{p}}$, so that $\boldsymbol{b}(\boldsymbol{x}) = \boldsymbol{b}(\boldsymbol{p}\cdot\boldsymbol{x}) = \boldsymbol{b}(\lambda)$. The functional form $\boldsymbol{b}(\lambda)$ is arbitrary, provided that it satisfies the constraints $\nabla\cdot\boldsymbol{b} = 0$, $\overline{\boldsymbol{b}} = 0$, and $B = \text{const}$. Using $\nabla\cdot\boldsymbol{b} = \boldsymbol{p}\cdot d\boldsymbol{b}/d\lambda = 0$, which implies $\hat{\boldsymbol{p}}\cdot\boldsymbol{b} = 0$ via $\overline{\boldsymbol{b}} = 0$, we see that $\boldsymbol{b}$ has two independent nonzero components. We choose these to be in the $\hat{\boldsymbol{n}} = (\hat{\boldsymbol{p}}\times\hat{\boldsymbol{v}}_\mathrm{A})/|\hat{\boldsymbol{p}}\times\hat{\boldsymbol{v}}_\mathrm{A}|$ direction (the perturbation direction of a linear Alfvén wave) and the $\hat{\boldsymbol{m}} = (\hat{\boldsymbol{p}}\times\hat{\boldsymbol{n}})/|\hat{\boldsymbol{p}}\times\hat{\boldsymbol{n}}|$ direction. Defining $b_n = \hat{\boldsymbol{n}}\cdot\boldsymbol{b}$ and $b_m = \hat{\boldsymbol{m}}\cdot\boldsymbol{b}$, we see that the parallel field perturbation — that which can lead to switchbacks — is

$$b_\parallel = \hat{\boldsymbol{v}}_\mathrm{A}\cdot\boldsymbol{b} = \hat{\boldsymbol{v}}_\mathrm{A}\cdot\hat{\boldsymbol{m}}\,b_m = b_m\sin\vartheta. \tag{2}$$

We are interested in relating $b_\parallel/v_\mathrm{A}$, the relative parallel-field perturbation, to the wave's amplitude

$$A \equiv \frac{|\boldsymbol{b}|}{v_\mathrm{A}} = \frac{1}{v_\mathrm{A}}\sqrt{b_n^2 + b_m^2}. \tag{3}$$

A simple argument from M+21 (see also Refs. [21, 25]) goes as follows. First, note that the constant-B condition,

$$\frac{B^2}{4\pi\rho} = v_{\mathrm{A}p}^2 + b_n^2 + (b_m + v_{\mathrm{A}m})^2 \tag{4}$$

(where $v_{\mathrm{A}p} = \hat{\boldsymbol{p}}\cdot\boldsymbol{v}_\mathrm{A}$ and $v_{\mathrm{A}m} = \hat{\boldsymbol{m}}\cdot\boldsymbol{v}_\mathrm{A}$), implies $A^2/\sin^2\vartheta + 1 + 2b_m/v_{\mathrm{A}m} = \text{const}$. on dividing by $v_{\mathrm{A}m}^2$. Taking the spatial average and multplying by $\sin^2\vartheta$ fixes the constant, thus allowing one to solve for b_m to find $b_\parallel/v_\mathrm{A} = (\overline{A^2} - A^2)/2$. This shows that for $A \ll 1$, $b_\parallel/v_\mathrm{A}$ scales with the wave amplitude squared. On the other hand, the amplitude definition (3) shows that $b_m/v_\mathrm{A} \lesssim A$, so that for $A \gtrsim 1$, $b_\parallel/v_\mathrm{A} \lesssim A\sin\vartheta$, with approximate equality for $b_m \approx b_n$. Combined, these constraints give

$$\frac{b_\parallel}{v_\mathrm{A}} \sim \min\left\{A^2, A\sin\vartheta\right\}, \tag{5}$$

which we find is very well satisfied by constant-B 1-D solutions. Note that in using Eq. (5), A and $b_\parallel$ are simply numbers rather than functions of λ (i.e., A is loosely equated with its spatial average, $A \sim \overline{A}$), a distinction that should be clear from context in the discussion below. We see that large-amplitude waves, with $A \gtrsim \sin\vartheta$, preferentially form switchbacks ($b_\parallel \gtrsim v_\mathrm{A}$) when they are oblique ($\sin\vartheta \approx 1$). Unsurprisingly, waves with $A \ll \sin\vartheta$ can never form switchbacks, because, given that $\sin\vartheta < 1$, the A^2 scaling only ever applies for $A \lesssim 1$ (implying $b_\parallel \lesssim v_\mathrm{A}$).

The result (5) can be simply explained intuitively as follows: field perturbations are confined to be perpendicular to $\boldsymbol{p}$ by $\nabla\cdot\boldsymbol{B} = 0$, so $b_\parallel$ perturbations are necessarily small when $\boldsymbol{p}$ and $\boldsymbol{v}_\mathrm{A}$ are nearly parallel; additionally, in large-amplitude waves, b_n causes large variation in B, which must be compensated by a similar-magnitude b_m component. Thus, large switchbacks result from large-amplitude, oblique nonlinear Alfvén waves. Importantly, as discussed by M+21 this provides a simple explanation for the observed radial elongation of switchbacks [26, 27]: in a random magnetic field with power spread across a wide range of wavenumbers, only preferentially perpendicular (radially elongated) structures generate significant $b_\parallel$, even for $A \gtrsim 1$.

B. Constant-B wave solutions

A question that naturally arises, and one that will be important for our analysis later in this manuscript, is how to form constant-B solutions. In general, this is simple in one dimension for small-amplitude perturbations, but not for larger amplitudes, and not in two or three dimensions (see, e.g., Refs. 28–30 and J+22). In one dimension, one can simply arbitrarily specify the functional form of $b_n(\lambda)$, then solve Eq. (4) for b_m:

$$b_m = -v_{\mathrm{A}m} + \sqrt{\frac{B^2}{4\pi\rho} - v_{\mathrm{A}p}^2 - b_n^2}. \tag{6}$$

In doing so, one must enforce $\overline{b_m} = 0$ (otherwise b_m would contribute to $\boldsymbol{v}_\mathrm{A}$), which is used as a constraint to solve for the unknown constant field magnitude B^2. But, Eq. (6) does not always have real solutions for an arbitrary choice of b_n, which leads to an effective amplitude limit on constructing such a wave for the chosen functional form of b_n. For example, Ref. 21 show that if b_n is chosen as sinusoidal, with $b_n = A_n\sin(k\lambda)$, solutions on a single branch of the square root exist only for $A_n < (\pi/2)\sin\vartheta$.

However, this amplitude limit is artificial: it arises because the constant-B requirement constrains the functional form of both b_n and b_m simultaneously, meaning b_n cannot be chosen arbitrarily. If b_n is chosen correctly, it is perfectly possible to form smooth constant-B waves of arbitrary amplitude for arbitrary ϑ. Below, we discuss how to do this by starting a with lower-amplitude wave, for which one can solve Eq. (6), then growing it via expansion using the asymptotic theory of M+21 (see Eq. (7)). Such a process is also physical: Refs. 21 and 31 showed that, no matter how large it becomes, the average amplitude $\overline{A}$ of a spherically polarized 1-D wave grows due to plasma expansion in exactly the same way as does a linear ($A \ll 1$) Alfvén wave. Thus, starting from small amplitudes in the lower solar atmosphere, and neglecting the influence of turbulence and parametric decay, waves can in principle grow to $A \gtrsim 1$, so long as both b_n and b_m change shape in order to allow a consistent solution with constant B.

C. Wave evolution and growth with expansion

M+21 consider 1-D wave evolution in the MHD expanding-box model (EBM) [32], which describes the evolution of a small patch of plasma in a spherically expanding wind with

constant velocity U. We do not reproduce the full equations here (see J+22), but just note that the model is parameterised by the expansion parameter a, which starts at $a = 1$ at some reference radius R_0 and evolves as $a = 1 + \dot{a}t$, where $\dot{a}/a = U/R = U/(R_0 + Ut)$ is the expansion rate ($\dot{a} = U/R_0$ is constant). The perpendicular dimensions of a plasma parcel scale $\propto a$, due to the spherical expansion, while the parallel dimension remains constant. Thus, the wavevector scales as $\boldsymbol{p} = (p_x, p_y, p_z) = (p_{x0}, a^{-1}p_{y0}, a^{-1}p_{z0})$, where $\boldsymbol{p}_0 = \boldsymbol{p}(a = 1)$ (with components p_{i0}). Due to magnetic flux and mass conservation, the Alfvén speed evolves with expansion according to $\boldsymbol{v}_\mathrm{A} = (v_{\mathrm{A}x}, v_{\mathrm{A}y}, v_{\mathrm{A}z}) = (a^{-1}v_{\mathrm{A}x0}, v_{\mathrm{A}y0}, v_{\mathrm{A}z0})$ where $\boldsymbol{v}_{\mathrm{A}0} = \boldsymbol{v}_\mathrm{A}(a = 1)$. The different scalings of the radial and perpendicular components of $\boldsymbol{v}_\mathrm{A}$ cause the mean-field direction to rotate with a and is the manifestation of the Parker spiral within this simplified model. High frequency waves, those with frequency $\omega_\mathrm{A} \gg \dot{a}/a$ (termed the WKB regime), change in amplitude according to $|\overline{\boldsymbol{b}}| \propto a^{-1/2}$, independently of the wave propagation direction (see App. C). Combined with the scaling of $\boldsymbol{v}_\mathrm{A}$, this leads to the well-known result that $\overline{A} \propto a^{1/2}$ in a radial background field, which, as mentioned above, applies for both linear and nonlinear waves ($A \gtrsim 1$). Note that, by assuming a constant U, the EBM applies only to radii where $U \gg v_\mathrm{A}$, outside the Alfvén radius R_A; inner regions with $R \lesssim R_\mathrm{A}$ exhibit some very important differences as concerns switchback formation, but are more complex to study in detail. See, e.g., §IID of J+22 for further discussion.

M+21 derive a simple equation that captures the slow growth and evolution of $\boldsymbol{b}(\lambda)$ due to constant expansion. The method involves using an asymptotic expansion in $\varepsilon = (\dot{a}/a)/(\boldsymbol{p}\cdot\boldsymbol{v}_\mathrm{A})$, which is the ratio of the expansion rate to the wave frequency $\omega_A = \boldsymbol{p}\cdot\boldsymbol{v}_\mathrm{A}$; $\varepsilon \ll 1$ implies the waves are in the WKB regime (note that ε remains constant during expansion because $\omega_A \propto a^{-1}$). Averaging over the fast wave motion, they obtain

$$\frac{\partial \boldsymbol{b}}{\partial t} + \frac{\dot{a}}{2a}\left(\boldsymbol{b} + 2\hat{\boldsymbol{p}}\hat{p}_x b_x\right) + \frac{\varepsilon}{2}\frac{\partial}{\partial\lambda}\left[\boldsymbol{p}\cdot\boldsymbol{u}_1\left(\boldsymbol{v}_\mathrm{AT} + \boldsymbol{b}\right)\right], \qquad (7)$$

where $\boldsymbol{v}_\mathrm{AT} \equiv \boldsymbol{v}_\mathrm{A} - \hat{\boldsymbol{p}}\hat{\boldsymbol{p}}\cdot\boldsymbol{v}_\mathrm{A}$ is the transverse part of the mean field. The evolution is closed by specifying $\boldsymbol{p}\cdot\boldsymbol{u}_1$, which is the (higher-order) compressive flow that is responsible for changing the shape of $\boldsymbol{b}$ to maintain constant B; it is given by

$$\boldsymbol{p}\cdot\frac{\partial \boldsymbol{u}_1}{\partial\lambda} = -\omega_A\frac{2b_x(v_{\mathrm{A}x} + \hat{p}_x\hat{\boldsymbol{p}}\cdot\boldsymbol{v}_\mathrm{A}) - \boldsymbol{b}\cdot\boldsymbol{v}_\mathrm{A}}{|\boldsymbol{v}_\mathrm{AT} + \boldsymbol{b}|^2}. \qquad (8)$$

Wave amplitude growth is contained in the second term in Eq. (7) (coupled with the scaling of $\boldsymbol{v}_\mathrm{A}$), which implies $|\overline{\boldsymbol{b}}| \propto a^{-1/2}$ as expected. In addition, M+21 derive equations for the higher-order density and B^2 fluctuations that are driven as part of this process, but these will not feature in our discussion.

Later in this work, we examine the properties of solutions to Eqs. (7) and (8) by means of its numerical solution. For this, we use a standard Fourier pseudospectral method with fourth- and fifth-order Runga-Kutta timestepping and 1024 grid points in λ. We also provide some cursory comparisons of the solutions Eqs. (7) and (8) with true MHD solutions in App. B, finding mostly good agreement except for a specific case where Eq. (7) seems to break down (it fails to maintain constant B).

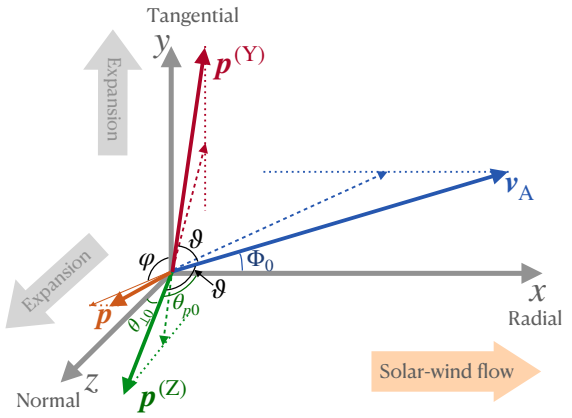

FIG. 1. The geometry and notation used to describe 1-D wave evolution from expansion in a Parker spiral. The mean field $\boldsymbol{v}_\mathrm{A}$ (blue) and wavevector $\boldsymbol{p}$ (red, green, and orange) evolve according to the EBM scalings described in § II C, as shown by the dashed arrows and dotted lines. Wave properties differ significantly depending on the direction of $\boldsymbol{p}$ compared to the plane of the Parker spiral, which we parametrize with angle φ, with the extreme cases $\hat{\boldsymbol{p}}^{(\mathrm{Y})}$ and $\hat{\boldsymbol{p}}^{(\mathrm{Z})}$ ($\varphi = 0$ or π, and $\varphi = \pm\pi/2$, respectively) plotted in Fig. 2. The angle between $\boldsymbol{v}_\mathrm{A}$ and $\boldsymbol{p}$ plays a key role in determining switchback properties and is denoted by ϑ.

Finally, it is worth noting that Eqs. (7) and (8) provide a convenient and practical method to construct large-amplitude Alfvénic solutions when the method described above (§ II B) fails at large A. One simply starts with a chosen form of $\boldsymbol{b}(\lambda)$ at smaller A, then evolves it according to Eqs. (7) and (8) to reach any desired amplitude. This process demonstrates that in one dimension at least, the apparent limits on A for some chosen form of b_n are artificial; in all choices for b_n that we have tried, waves grow to arbitrary amplitude without forming discontinuities.

III. SWITCHBACK FORMATION DUE TO EXPANSION

In this section, we study the evolution of 1-D Alfvén waves in an expanding plasma using the simple analytic scalings of $b_\parallel$ and A outlined above (§ II C). Throughout, we will heuristically equate $b_\parallel/v_\mathrm{A}$ with the "prevalence" of switchbacks, estimating how the this evolves due to expansion using Eq. (5). Correspondingly, we will regard A as a number (evolving with a) rather than a function of λ throughout this section. We will consider the wave to exhibit strong switchbacks once $b_\parallel/v_\mathrm{A} \gtrsim 1$, which (as we will see below) is actually a rather conservative estimate in some regimes because the volume filling fraction of large-$b_\parallel$ deviations can evolve to be quite small.

While we will find that the influence of the Parker spiral on switchbacks can be quite dramatic, it is worth cautioning the detailed results of this section (e.g., the exact form of $b_\parallel(a)$) may be of limited applicability to a real plasma. In particu-

lar, they apply only in the absence of turbulence, which both causes energy decay (thus changing the amplitude scalings) and acts to populate different wavenumbers $\boldsymbol{p}$ (thus invalidating the assumed wave angle ϑ evolution). Nonetheless, we will be able to draw some more general conclusions, which seem to match key results from 3-D nonlinear EBM simulations (J+22). These issues will be appraised in detail in § V; for now, we simply take as given the applicability of 1-D wave scalings and examine their consequences.

A. Switchback growth in a radial field

Before considering the evolution of waves in a Parker spiral, it is helpful to examine the radial-field case to better understand its important features. In this case, $\boldsymbol{v}_{\rm A} = a^{-1}v_{{\rm A}x}\hat{\boldsymbol{x}}$, so $A = A_0 a^{1/2}$, where A_0 is the initial amplitude at $a = 1$. We take $\boldsymbol{p}(a) = p_0(\cos\theta_{p0}, 0, a^{-1}\sin\theta_{p0})$, where θ_{p0} is the initial angle between the radial direction and the wave, which we have arbitrarily taken to lie in the x,z plane. We also define $\theta_p \equiv \tan^{-1}(p_z/p_x) = \tan^{-1}(a^{-1}\tan\theta_{p0})$ as the a-dependent evolution of this angle. To obtain simple, physically intuitive results, we imagine starting with a nearly perpendicular wave $\theta_{\perp 0} = \pi/2 - \theta_{p0} \ll 1$, and treat $\theta_{\perp 0} \ll 1$ as a small expansion parameter (see Fig. 1).

Using $\vartheta = \theta_p$ in Eq. (5) then expanding in $\theta_{\perp 0} \ll 1$ gives

$$\sin^2\vartheta = \frac{1}{1 + a^2\tan^2\theta_{\perp 0}} \approx \frac{1}{1 + a^2\theta_{\perp 0}^2}, \tag{9}$$

which shows $\sin\vartheta \simeq 1$ for $a \ll 1/\theta_{\perp 0}$ ($\theta_p \gtrsim 1$; mostly oblique propagation) and $\sin\vartheta \propto 1/a$ for $a \gg 1/\theta_{\perp 0}$ ($\theta_p \lesssim 1$; mostly parallel propagation). Thus, combined with the continual increase of $A \propto a^{1/2}$, we see that $b_\parallel/v_{\rm A}$ grows as $b_\parallel/v_{\rm A} \propto a$ for $a \ll 1/\theta_{\perp 0}$, or as $b_\parallel/v_{\rm A} \propto a^{1/2}$ if $b_\parallel/v_{\rm A} \gtrsim 1$. Then, it reaches a maximum at $a \approx 1/\theta_{\perp 0}$, before decreasing as $b_\parallel/v_{\rm A} \propto a^{-1/2}$ for $a \gg 1/\theta_{\perp 0}$ even though A continues to increase. The cause of the transition between these regimes is simply the transition from oblique ($\vartheta = \theta_p \gtrsim 1$) to parallel propagation ($\vartheta \lesssim 1$), which necessarily implies small $b_\parallel$ perturbations. The decrease in $b_\parallel/v_{\rm A}$ once $\vartheta \gtrsim 1$ also implies that A_0 must satisfy $A_0^2 \gtrsim \theta_{\perp 0}$ in order to form switchbacks at all – i.e., for $A_0^2 \lesssim \theta_{\perp 0}$, $b_\parallel/v_{\rm A}$ reaches a maximum value $b_\parallel/v_{\rm A} \lesssim 1$ before decreasing again.

An example $b_\parallel/v_{\rm A}$ evolution, which involves each of the regimes discussed above, is illustrated in Fig. 2 with the thick black lines.

B. Switchback growth in the Parker Spiral

In the presence of a perpendicular component to the mean field (the Parker spiral), the scalings described above become more complex and interesting because of non-monotonic behavior of $\sin\vartheta$ and A. First, let us consider the amplitude evolution. We take the Parker spiral to lie in the x,y plane, $\boldsymbol{v}_{\rm A0} = v_{\rm A0}(\cos\Phi_0, \sin\Phi_0, 0)$, which implies that the radial (R), tangential (T), and normal (N) directions correspond to x, y, and z, respectively (see Fig. 1). We define $0 < \Phi_0 \ll 1$ as the initial Parker Spiral angle, which (like $\theta_{\perp 0}$) will be considered a small parameter and used to simplify the results. We also define the a-dependent Parker spiral angle $\Phi \equiv \tan^{-1}(v_{{\rm A}y}/v_{{\rm A}x}) = \tan^{-1}(a\tan\Phi_0)$. Using $\boldsymbol{v}_{\rm A} = v_{\rm A0}(a^{-1}\cos\Phi_0, \sin\Phi_0, 0)$ and $\overline{|\boldsymbol{b}|} \propto a^{-1/2}$ gives,

$$A \approx \frac{A_0 a^{-1/2}}{\sqrt{a^{-2}\cos^2\Phi_0 + \sin^2\Phi_0}} \approx \frac{A_0 a^{1/2}}{\sqrt{1 + a^2\Phi_0^2}}, \tag{10}$$

showing that A grows like the radial-field case, $A \propto a^{1/2}$, for $\Phi \lesssim 1$ ($a \lesssim 1/\Phi_0$), but starts decreasing $A \propto a^{-1/2}$ once $\Phi \gtrsim 1$ ($a \gtrsim 1/\Phi_0$) because the mean field decays more slowly than the wave-like perturbations.

We must now allow $\boldsymbol{p}$ to have components in all three directions to capture the full range of possible behaviors of $\sin\vartheta$. We thus parameterize it with $\boldsymbol{p}(a) = p_0(\cos\theta_{p0}, a^{-1}\sin\theta_{p0}\cos\varphi, a^{-1}\sin\theta_{p0}\sin\varphi)$, so that $\varphi = \pm\pi/2$ corresponds to $\boldsymbol{p}$ lying in the plane perpendicular to the Parker spiral mean field, and $\varphi = 0$ or π corresponds to $\boldsymbol{p}$ lying in the same plane as the Parker spiral. We will sometimes describe these cases as $\hat{\boldsymbol{p}}^{(\rm Z)}$ and $\hat{\boldsymbol{p}}^{(\rm Y)}$, respectively, as illustrated with the green and red arrows in Fig. 1. We again imagine starting from a highly oblique wave ($\theta_{\perp 0} = \pi/2 - \theta_{p0} \ll 1$, also with $|\vartheta| < \pi/2$) and compute

$$\sin^2\vartheta = 1 - \frac{(\boldsymbol{p}\cdot\boldsymbol{v}_{\rm A})^2}{|\boldsymbol{p}|^2|\boldsymbol{v}_{\rm A}|^2} \tag{11}$$

as a function of a. The result is that $\sin\vartheta$ decreases in the same way as radial-$\boldsymbol{v}_{\rm A}$ case initially, but its evolution starts to differ markedly as a approaches

$$a_{\vartheta_{\rm min}} = \sqrt{\cot\theta_{\perp 0}\cot\Phi_0} \approx \frac{1}{\sqrt{\theta_{\perp 0}\Phi_0}}, \tag{12}$$

at which point $\sin\vartheta$ reaches a local minimum

$$\begin{aligned}\sin^2\vartheta_{\rm min} &= 1 - \frac{(\sin\Phi_0\cos\theta_{\perp 0}\cos\varphi + \cos\Phi_0\sin\theta_{\perp 0})^2}{\sin^2(\Phi_0 + \theta_{\perp 0})} \\ &\approx 1 - \frac{(\Phi_0\cos\varphi + \theta_{\perp 0})^2}{(\theta_{\perp 0} + \Phi_0)^2}.\end{aligned} \tag{13}$$

From this point, unlike the radial case, $\sin\vartheta$ starts increasing again back towards oblique propagation, because $\boldsymbol{v}_{\rm A}$ rotates towards the perpendicular direction.

We illustrate the effect of these features on the evolution of Eq. (5) in Fig. 2, using Eqs. (10) and (11) for A and $\sin\vartheta$. All curves have the same initial $\vartheta = 80^\circ$, and the different colors show a variety of initial Parker spiral angles Φ_0. Note that θ_{p0} must be adjusted to keep fixed initial ϑ while varying Φ_0, which implies $\theta_{p0} = \cos^{-1}(\cos\vartheta/\cos\Phi_0)$ for $\varphi = \pm\pi/2$, or $\theta_{p0} = \vartheta\cos\varphi + \Phi_0$ for $\varphi = 0$ or π. We plot the waves with $\varphi = \pm\pi/2$ ($\hat{\boldsymbol{p}}^{(\rm Z)}$) and with $\varphi = 0, \pi$ ($\hat{\boldsymbol{p}}^{(\rm Y)}$) separately in the two panels, because their evolution differs significantly and this will suggest important conclusions about switchback properties. In order to understand the illustrated behavior, let

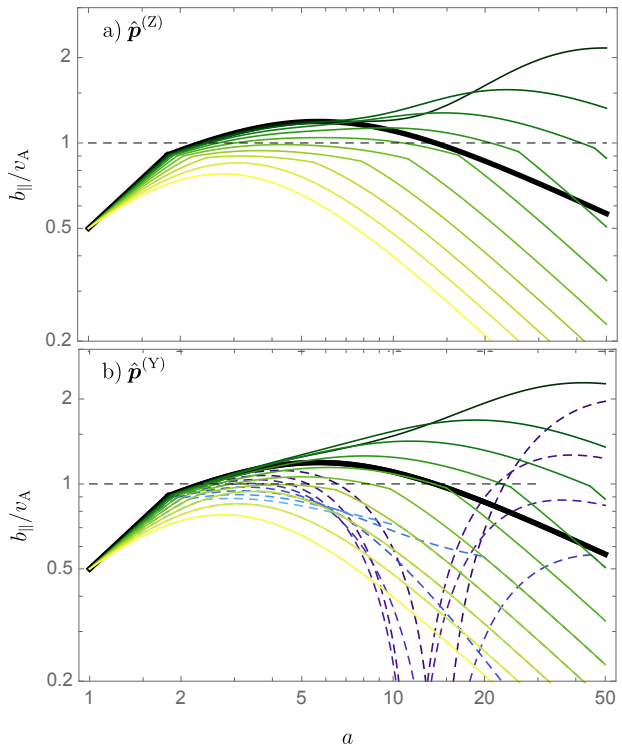

FIG. 2. Evolution of the parallel-field perturbation, roughly equatable with the switchback prevalence, computed from Eq. (5) using the EBM scalings of A and ϑ. In all cases we start from $\vartheta = \pm 80^\circ$ and A_0=0.8; thick black lines show the radial-$\boldsymbol{v}_\mathrm{A}$ case ($\Phi_0 = 0$), and colored lines show that with a Parker Spiral with $\Phi_0 = 2^\circ, 4^\circ, \ldots, 20^\circ$ from dark green to light yellow, or dark blue to light blue. Panel (a) shows $\varphi = \pm\pi/2$, where $\boldsymbol{p}$ lies in the x,z plane ($\hat{\boldsymbol{p}}^{(\mathrm{Z})}$ in Fig. 1), while panel (b) shows $\varphi = \pi$ in solid green-yellow lines and $\varphi = 0$ in dashed blue lines (in both these cases $\boldsymbol{p}$ lies in the x,y plane; $\hat{\boldsymbol{p}}^{(\mathrm{Y})}$ in Fig. 1). For $\varphi = 0$, the wave passes through purely parallel propagation at $a = a_{\vartheta_\mathrm{min}}$ (Eq. (12)), implying $b_\parallel/v_\mathrm{A} = 0$.

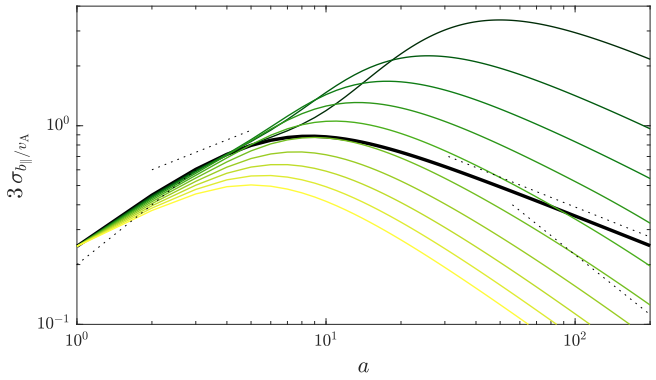

FIG. 3. Measured switchback prevalence computed from three times the standard deviation of $b_\parallel/v_\mathrm{A}$, $\sigma_{b_\parallel/v_\mathrm{A}} = [\overline{(b_\parallel - \overline{b_\parallel})^2}]^{1/2}/v_\mathrm{A}$, for 1-D waves evolved according to Eqs. (7) and (8). The color scheme is the same as Fig. 2, and we take $\boldsymbol{p}$ to lie in the x,z plane ($\varphi = \pi/2$). The dashed lines show the scalings, from left to right, a^1, $a^{1/2}$, $a^{-1/2}$, and a^{-1}, which are the theoretical expectations for the different regimes discussed in § III B. Clearly, aside from a modest vertical offset, which arises from the ambiguity of the definition of $b_\parallel/v_\mathrm{A}$ in Eq. (5), the simple computations of Fig. 2 give an extremely good match to the behavior of real 1-D waves (note the extended horizontal axis compared to Fig. 3).

us first consider the importance of the two angles Φ_0 and $\theta_{\perp 0}$ (controlling the Parker spiral and the wave's obliquity, respectively), then consider the wave's orientation φ.

For $\theta_{\perp 0} \gtrsim \Phi_0$ — i.e., when the Parker Spiral makes a smaller angle to the radial than the wavevector makes to the perpendicular — $a_{\vartheta_\mathrm{min}} < 1/\Phi_0$. This means $\sin\vartheta$ reaches its minimum and starts increasing again before A starts decreasing at $\Phi = 45^\circ$ ($a \sim 1/\Phi_0$; see Eq. (10)), but after the maximum of $b_\parallel/v_\mathrm{A}$ for the radial-$\boldsymbol{v}_\mathrm{A}$ waves at $a \sim 1/\theta_{\perp 0}$. This explains the inflection points seen in the green curves in Fig. 2: $\sin\vartheta$ decreases significantly below unity by $a \sim 1/\theta_{\perp 0}$ when $\theta_p \lesssim 1$, then reaches its minimum at $a \sim 1/\sqrt{\theta_{\perp 0}\Phi_0}$ causing $b_\parallel/v_\mathrm{A}$ to start increasing again; but then A itself starts decreasing at $a \sim 1/\Phi_0$ causing $b_\parallel/v_\mathrm{A}$ to decrease. Thus, in this regime of modestly oblique waves $\theta_{\perp 0} \gtrsim \Phi_0$, switchbacks usually form significantly more efficiently than in the radial-$\boldsymbol{v}_\mathrm{A}$ case, because the waves evolve to become more oblique after $\hat{\boldsymbol{p}}$ rotates to be mostly radial, but before the Parker spiral rotates past $\simeq 45^\circ$. In contrast, in the opposite regime of a large Parker spiral with $\theta_{\perp 0} \lesssim \Phi_0$ (yellow curves in Fig. 2), A starts decreasing, at $a \approx 1/\Phi_0 \lesssim a_{\vartheta_\mathrm{min}}$, before the minimum in $\sin\vartheta$. Because $\sin\vartheta_\mathrm{min} \approx 1$ in this regime unless $\cos\varphi \approx 1$ (see Eq. (13)), $b_\parallel/v_\mathrm{A} \sim \min(A, A^2)$, which simply peaks when $\Phi \sim 1$ then decreases again, making for inefficient switchback formation even though the wave remains oblique at all times. In both regimes, the decrease $A \propto a^{-1/2}$ always wins out and causes $b_\parallel/v_\mathrm{A}$ to decrease as $b_\parallel/v_\mathrm{A} \propto a^{-1}$ once $\Phi \gtrsim 1$ and $A \lesssim 1$, which is faster than in the radial-$\boldsymbol{v}_\mathrm{A}$ case.

As seen by the comparison between panels (a) and (b) of Fig. 2, the wave's direction φ is also key in determining its evolution. For $\cos\varphi \neq 1$, as applies to $\hat{\boldsymbol{p}}^{(\mathrm{Z})}$ waves or when $\hat{\boldsymbol{p}}$ and $\boldsymbol{v}_\mathrm{A}$ lie in the same plane but different quadrants ($\varphi = \pi$), the evolution occurs broadly as described above, with $\varphi = \pi$ having a modestly larger $\sin\vartheta_\mathrm{min}$ and thus slightly larger $b_\parallel/v_\mathrm{A}$ for intermediate times (c.f. green-yellow curves in panels (a) and (b)). However, for $\varphi = 0$, $\hat{\boldsymbol{p}}$ and $\boldsymbol{v}_\mathrm{A}$ pass through each other at $a_{\vartheta_\mathrm{min}}$, *viz.,* the wave becomes perfectly parallel with $\vartheta = 0$ (this effect can be seen clearly by following the dotted red and blue lines in Fig. 1). At this point, $b_\parallel/v_\mathrm{A}$ must go to zero, and ϑ flips sign. Although $\sin\vartheta$ then increases rather rapidly in the opposite direction, we see that for most of these wave's evolution, they produce only small $b_\parallel/v_\mathrm{A}$ fluctuations. Thus, the Parker spiral can create strong differences between switchback properties, depending on the direction of fastest variation ($\hat{\boldsymbol{p}}$) of the wave or structure in question.

Finally, we note that in order for any physics related to $\sin\vartheta$ to be relevant, the maximum of $b_\parallel/v_\mathrm{A}$ should occur when $A^2 \gtrsim A\sin\vartheta$ (see Eq. (5)). This implies a minimum initial wave amplitude $A_0 \sim a_{\vartheta_\mathrm{min}}^{-1/2}\sin\vartheta_\mathrm{min}$, below which $b_\parallel/v_\mathrm{A} \sim A^2$ for all a and there are no significant switchbacks ($b_\parallel/v_\mathrm{A} \lesssim 1$).

1. Comparison to wave solutions

The above arguments and Fig. 2 are based purely on Eq. (5). How well do these estimates compare to true expanding wave solutions? To test this, we solve Eqs. (7) and (8) starting from random initial conditions constructed from the first 10 Fourier modes with $\vartheta = 80^\circ$ and $\varphi = \pi/2$, varying Φ_0 in order to match the computations Fig. 2(a). Results are shown in Fig. 3. The definition of $b_\parallel/v_\mathrm{A}$ is only valid as a scaling in Eq. (5), so to make a reasonable comparison we measure the standard deviation of $b_\parallel/v_\mathrm{A}$ across the domain, with $b_\parallel(\lambda) = \boldsymbol{b}\cdot\hat{\boldsymbol{v}}_\mathrm{A}$. The agreement, both in the general form and the predicted scalings with a (dotted black lines), is extremely good, including in features such as the inflection point, which one might have expected to be an artefact of the idealised nature of Eq. (5). The spatial form of the solutions themselves are shown in Fig. 4 for $\Phi_0 = 2^\circ$ and Fig. 5 for $\Phi_0 = 0$ (radial $\boldsymbol{v}_\mathrm{A}$) and will discussed in detail below. In addition, we show in App. B (see Fig. 8) that the solutions of Eq. (7) match true 2-D expanding MHD solutions very well.

In Fig. 3, we do not consider waves with $\varphi = 0$ or π, for which $b_\parallel$ estimates are shown in Fig. 2(b). The reason for this is that Eqs. (7) and (8) fail to produce constant-B solutions when $\varphi = 0$ or π. Although the cause for this behavior remains unclear (we speculate that it results from the more rapid evolution of $\sin\vartheta$ in this geometry), it is important to note that Eq. (7) was derived assuming constant B, so if this is not satisfied we should not trust its solutions. Thus, it is not worthwhile to compare to the predictions of Eq. (5) and Fig. 2(b) in detail. The consequences of this discrepancy are discussed below (§ III C 1) and in App. B (see Fig. 9 for MHD solutions of this geometry).

C. Consequences for the solar wind

Although we will delay detailed discussion of turbulence and 3-D fields until § V, it is helpful to briefly outline some possible observable consequences of these wave properties for switchbacks in the solar wind. The most obvious property from Fig. 2 is that a modest Parker spiral, with $\Phi \lesssim 1$ ($v_{\mathrm{A}x} > v_{\mathrm{A}y}$) can significantly enhance switchback formation. This is because, when $\theta_{\perp 0} \gg \Phi_0$ (with $\theta_{\perp 0} = \pi/2 - \theta_{p0} \simeq \pi/2 - \vartheta_0$ in most regimes) the simultaneous rotation of $\boldsymbol{v}_\mathrm{A}$ and $\boldsymbol{p}$ causes the wave obliquity to increase even when $\Phi \ll 1$. This seems to be the more relevant regime for the solar wind, since we measure Φ to be rather small near R_A (where the EBM becomes applicable), and there are a wider range of wavenumbers with $\theta_{\perp 0} \gtrsim \Phi_0$ than with $\theta_{\perp 0} \lesssim \Phi_0$ if $\Phi_0 \ll 1$. Thus, we predict more robust growth of switchbacks due to expansion in the presence of a sub-45° Parker spiral than not, an observationally testable prediction that is also seen in the simulations of J+22.

Another interesting conclusion we can draw concerns the directions of switchback deflections. All else being equal, waves with $\boldsymbol{p}$ perpendicular to the plane of the Parker spiral ($\hat{\boldsymbol{p}}^{(\mathrm{Z})}$) generate more switchbacks than waves with $\boldsymbol{p}$ in the plane of the Parker spiral ($\hat{\boldsymbol{p}}^{(\mathrm{Y})}$): half of the $\hat{\boldsymbol{p}}^{(\mathrm{Y})}$ waves (those with $\varphi = 0$) evolve to become purely parallel and cause only small $b_\parallel/v_\mathrm{A}$ over a wide portion of their evolution. Because these are Alfvénic fluctuations, the strongest $\boldsymbol{b}$ fluctuation lies in the $\hat{\boldsymbol{n}} = (\hat{\boldsymbol{p}}\times\hat{\boldsymbol{v}}_\mathrm{A})/|\hat{\boldsymbol{p}}\times\hat{\boldsymbol{v}}_\mathrm{A}|$ direction, which means that $\hat{\boldsymbol{p}}^{(\mathrm{Z})}$ waves cause large b_y fluctuations, and $\hat{\boldsymbol{p}}^{(\mathrm{Y})}$ large b_z fluctuations. Thus, we expect switchbacks to preferentially involve rotations of the field in the plane of the Parker spiral (the tangential direction), rather than the normal direction. This seems to be observed, at least partially, in the simulations of J+22 (see their figure 7), and, more clearly in PSP observations [18, 26]. In essence, this argument is nothing more than the statement that for a distribution of waves with wavevectors that are biased towards the radial direction (as caused by expansion), wavevectors that lie in the plane perpendicular to the mean field are more oblique, on average, than those in the plane of the mean field. This interpretation is explored in more detail in App. A to provide another argument for this general effect.

1. The assumption of constant B for $\hat{\boldsymbol{p}}^{(\mathrm{Y})}$ waves

We noted above that when $\varphi = 0$ or π ($\hat{\boldsymbol{p}}^{(\mathrm{Y})}$), Eq. (7) fails to maintain a constant-B solution as the wave grows. This raises the obvious question of whether Eq. (5) is valid for such waves, and, if it is not, what will be the consequences. In App. B, we address this question by directly comparing solutions of Eq. (7) to 2-D expanding MHD solutions, finding that indeed Eq. (7) overpredicts the variation in B compared to MHD for this geometry, although the general form of the solutions is similar (see Fig. 9). However, we do still see tentative evidence that, even in MHD, larger variation in B occurs compared to a radial $\boldsymbol{v}_\mathrm{A}$ or $\varphi = \pm\pi/2$, particularly for $\varphi = \pi$ (which, recall, generates larger $b_\parallel$ than $\varphi = 0$). While a more careful study is needed, if this result holds, it only strengthens our main results from this section, implying that not only do $\hat{\boldsymbol{p}}^{(\mathrm{Y})}$ waves generate relatively smaller $b_\parallel$ because of the geometry of $\sin\vartheta$, they also generate larger B fluctuations that will then be more prone to dissipation by other means (e.g., kinetic damping or shocks). This would only act to enhance the dominance of b_y (tangential) over b_z (normal) rotations in switchbacks, strengthening our second conclusion above.

IV. THE STRUCTURE OF SWITCHBACKS IN THE TANGENTIAL PLANE

Above, we saw that the addition of a small Parker spiral can significantly enhance switchback generation, particularly when $\boldsymbol{p}$ lies in the x,z plane and $\boldsymbol{b}$ is dominated by its y component. In this section, we explore the structure of the wave solutions that develop under these conditions, governed by the constant-B constraint and the rotating mean field and wavevectors. We will show that in the regime where the Parker spiral significantly modifies switchbacks — i.e., as a approaches and exceeds $a_{\vartheta_\mathrm{min}}$ (Eq. (12)) — field rotations are generically "tangentially skewed": the deflection of $\boldsymbol{b}$ always causes b_x to increase, rather than decrease. This implies that

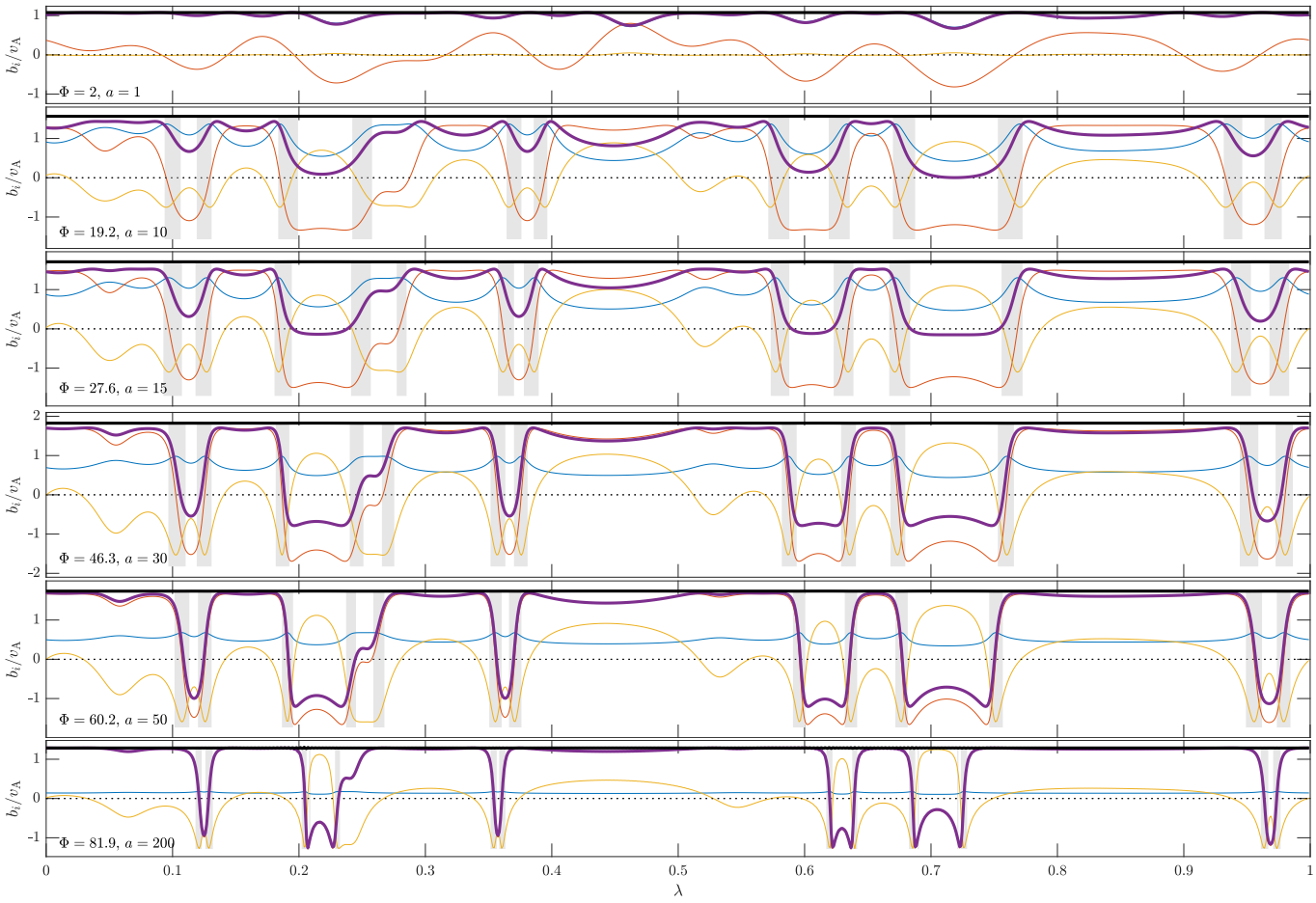

FIG. 4. An example of how a spherically polarized wave evolves in a background magnetic field with a Parker spiral, computed from Eqs. (7) and (8). The wave is similar to the darkest-green lines in Fig. 2a and 3, with $\Phi_0 = 2°$, initial $\vartheta = 80°$ (implying $a_{\vartheta_{\min}} \approx 12.7$), and $A_0 \approx 0.4$ formed from a random collection of the first 5 Fourier modes. In each panel, thin blue, red, and yellow lines show $b_x + v_{Ax}$, $b_y + v_{Ay}$, and b_z, respectively, each normalized to v_A. The thick black line shows $(B/\sqrt{4\pi\rho})/v_A$, and the thick purple line shows $b_\parallel/v_A + 1$, which is the normalized total field in the $\hat{\boldsymbol{v}}_A$ direction. We show panels of increasing a, as labelled in the bottom-left corner, with the vertical size of each panel scaled to the current total amplitude of the wave (i.e., the y-axis scale remains constant in units of b_i/v_A). The shaded grey regions in each panel highlight the regions of $b_\parallel$ with particularly sharp gradients — i.e., the switchback deflections — which we can see are generically associated with increases (rather than decreases) in b_x. This implies the $\boldsymbol{b}$ vector rotates in a tangentially skewed way in switchbacks, towards the v_{Ax} direction. In addition, we see that switchbacks become more and more intermittent as Φ increases: although the standard deviation of $b_\parallel$ starts decreasing for $a \gtrsim 50$ because A starts decreasing (c.f. Fig. 3), the relative size of individual deflections actually increases, while their volume filling fraction decreases.

through the switchback, the field deflects around towards the positive radial (v_{Ax}) direction (then past it), as opposed to the negative radial direction. We provide a simple proof for why this must occur based on certain assumptions about the form of such switchbacks and the $\nabla \cdot \boldsymbol{b} = 0$ and constant-B constraints. For simplicity of notation, we will assume v_{Ax} points in the $+\hat{\boldsymbol{x}}$ direction and v_{Ay} in the $+\hat{\boldsymbol{y}}$ direction; in the case with v_{Ax} in the $-\hat{\boldsymbol{x}}$ direction, $\boldsymbol{b}$ deflects towards the negative radial direction instead (i.e., still v_{Ax}), but is otherwise identical. We will also assume the wave starts with $\theta_{\perp 0} \gtrsim \Phi_0$, because the opposite (large-Parker-spiral) limit with $\theta_{\perp 0} \lesssim \Phi_0$ was shown above to be ineffective at generating switchbacks (it also requires extremely perpendicular waves for small Φ_0). Through this section we do not consider waves with $\varphi = 0$ or π ($\hat{\boldsymbol{p}}^{(Y)}$); this is both because constant-B solutions for such waves are not so easily understood (see § III C 1), and because field rotations will be more symmetric in this case anyway (since they are predominantly in the normal direction; see Fig. 9).

The evolution of a representative 1-D wave solution with a Parker spiral is shown in Fig. 4, starting from $\vartheta = 80°$, $\Phi_0 = 2°$, and $\varphi = \pi/2$, to match the parameters of the dark green solutions in Figs. 2(a) and 3. The equivalent solution without a Parker spiral, matching the black lines in Figs. 2(a) and 3, in is shown in Fig. 5 to provide a reference for comparison (see also M+21 figure 4). Similar to Fig. 3, the initial conditions are constructed using Eq. (6) with random amplitudes in the first 5 Fourier modes for $b_n = b_y$. We then evolve these according to Eqs. (7) and (8), capturing the change in shape of $\boldsymbol{b}$ needed to keep B constant as the wave grows due to ex-

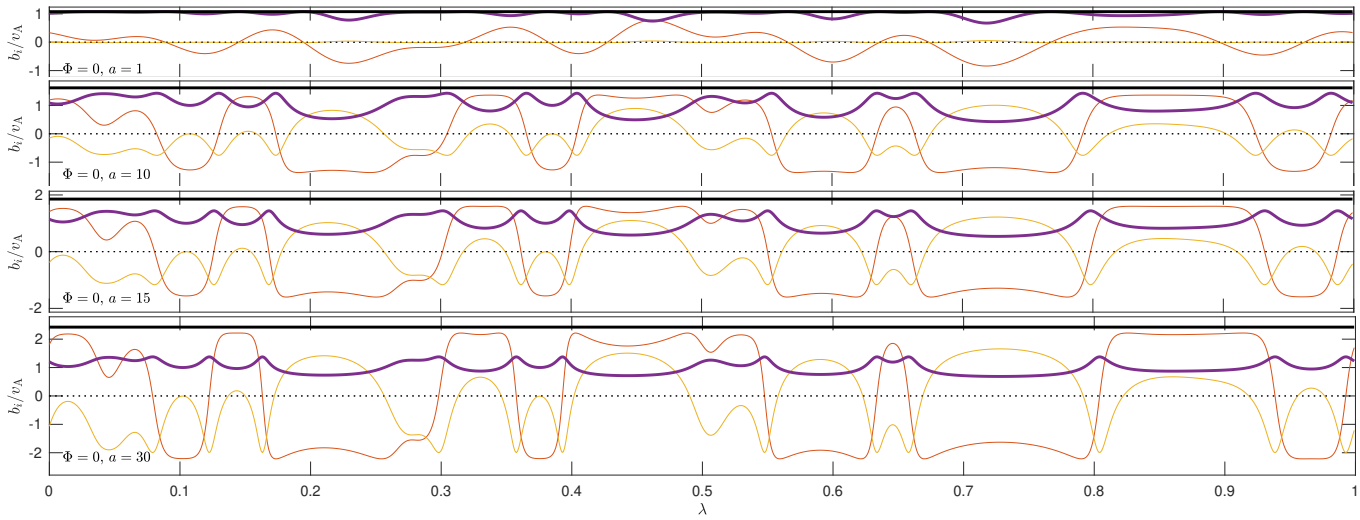

FIG. 5. As in Fig. 4, and with the same b_n used for the initial conditions, but with no Parker spiral ($\Phi = 0$). In this case, $b_\parallel = b_x$ so the purple line covers the blue line. The switchback prevalence starts decreasing once $a \gtrsim 10$, even though A continues to increase. Beyond this point, the wave form hardly changes shape as it grows because the mean field makes a relatively small contribution to the total B.

pansion. This initial condition, as expected, involves predominantly b_y perturbations (red line). Strong switchbacks (thick purple lines) develop at later times as expected from Fig. 2a. They are dominated by sudden changes in the direction of b_y and always involve an increase in b_x (blue lines) through the sharp change in $b_\parallel$ (grey shaded regions). This implies that the magnetic-field lines always rotate towards the positive radial direction during the field reversal, *viz.,* they are tangentially skewed. Switchbacks do not grow nearly as effectively in the radial-$\boldsymbol{v}_A$ case (Fig. 5).

A. A simple proof of switchback tangential skewness

To understand why this behavior occurs, let us first consider the regime in which it occurs. Because $b_\parallel = b_x\hat{v}_{Ax} + b_y\hat{v}_{Ay}$ must decrease below $\simeq -v_A$ to form a switchback, it must involve either a large-negative b_x or large-negative b_y (or both). The former case is simply a standard radial-$\boldsymbol{v}_A$ switchback as explored in M+21 and should not be expected to involve preferential deflections. This situation will apply even with a Parker spiral when $a \lesssim 1/\theta_{\perp 0}$ (i.e., when $\theta_p \gtrsim 45°$, which also implies $\Phi \ll 45°$), because such waves behave like the radial-$\boldsymbol{v}_A$ case anyway (see § III B). However, the latter case, with a large b_y perturbation, is different. As we now show, it takes over before or around $a \sim a_{\vartheta_{min}}$, which is well before $v_{Ay} \approx v_{Ax}$ ($\Phi \approx 45°$; see Eq. (12)). To understand why, we first note that $b_y \approx b_n$ and $b_m^2 \approx b_x^2 + b_z^2$ because $\boldsymbol{v}_A$ remains nearly radial, while $\boldsymbol{p}\cdot\boldsymbol{b} = 0$ implies

$$b_x = -\tan\theta_p b_z \tag{14}$$

(this can be clearly observed in the blue and yellow lines in Fig. 4). For $a \approx a_{\vartheta_{min}} \approx 1/\sqrt{\theta_{\perp 0}\Phi_0}$ and $\theta_{\perp 0} \gg \Phi_0$, we thus see $b_x \ll b_z \approx b_m$ implying $b_x \approx b_m\sqrt{\Phi_0/\theta_{\perp 0}}$. This shows that at $a \approx a_{\vartheta_{min}}$,

$$b_x\hat{v}_{Ax} + b_y\hat{v}_{Ay} \approx b_m\sqrt{\Phi_0/\theta_{\perp 0}} + b_n\sqrt{\Phi_0/\theta_{\perp 0}}, \tag{15}$$

where we have used the fact that $\hat{v}_{Ax} \approx 1$ and $\hat{v}_{Ay} \approx a\Phi_0 \approx \sqrt{\Phi_0/\theta_{\perp 0}}$ (because $\Phi \ll 1$ since $a_{\vartheta_{min}} \ll 1/\Phi_0$). Thus, since $b_n \gtrsim b_m$ (with near equality holding once $A \gtrsim 1$; see § II A), $b_y\hat{v}_{Ay}$ dominates for $a \gtrsim a_{\vartheta_{min}}$, meaning switchbacks result from large b_y fluctuations, rather than large b_x fluctuations, even though $\hat{v}_{Ax} > \hat{v}_{Ay}$ for a wide range of a after this point (until $a \lesssim 1/\Phi_0$). This behavior can be seen in the second ($a = 10$) panel of Fig. 4, which is pictured slightly before $a_{\vartheta_{min}} \approx 12.7$ for these parameters: at this a, some $b_\parallel$ minima are dominated by b_y fluctuations (e.g., around $\lambda \approx 0.1$), some are dominated by b_x fluctuations (e.g., around $\lambda \approx 0.45$), while the largest $b_\parallel$ perturbations involve both (e.g., around $\lambda \approx 0.7$). In contrast, by later times (e.g., the next panel where $\Phi \approx 30°$), $b_\parallel$ fluctuations are nearly completely determined by large changes in b_y to $b_y < 0$.

With this piece of information in hand — that the enhanced switchback formation from the Parker spiral involves switchbacks that are dominated by b_y perturbations — it is straightforward to demonstrate that b_x must increase through a switchback. First, we form the spatial constant

$$\Delta b^2 = (\boldsymbol{b} + \boldsymbol{v}_A)^2 - \boldsymbol{v}_A^2 = 2v_{Ax}b_x + 2v_{Ay}b_y + b_x^2\csc^2\theta_p + b_y^2, \tag{16}$$

which is the difference between the total and mean-field magnitude (we use Eq. (14) for b_z). Solving for b_x gives

$$\frac{b_x}{\sin^2\theta_p} = -v_{Ax} + \sqrt{v_{Ax}^2 + \csc^2\theta_p\left[\Delta b^2 + v_{Ay}^2 - (b_y + v_{Ay})^2\right]}. \tag{17}$$

Here, $\Delta b^2 + v_{Ay}^2$ is simply a positive constant, while $b_y + v_{Ay}$ is the total y-directed field. The key insight from Eq. (17) is that b_x is a monotonic function of $(b_y + v_{Ay})^2$ and is maximized when $(b_y + v_{Ay})^2 = 0$. Then, recall that $b_\parallel$ changes

are driven by $b_y\hat{v}_{\rm Ay}$, while $\hat{v}_{\rm Ay}$ is rather small, implying that any large change to $b_\parallel/v_{\rm A}$ must involve b_y, and thus $b_y+v_{\rm Ay}$, passing through zero (since b_y must also clearly remain less than the total field magnitude). Thus, any large change to $b_\parallel$ must occur around the same location as b_x being maximized, which implies that the magnetic-field vector rotates through the positive-radial direction during the switchback (note that b_x can subsequently decrease as b_y becomes large and negative and $(b_y+v_{\rm Ay})^2$ increases). This feature is highlighted by the grey shading in Fig. 4, which show the regions where $|db_\parallel/d\lambda|$ is near its maximum in each panel; clearly, such regions generically line up with positive peaks in b_x. Physically, all that Eq. (17) is saying is that the constant-B constraint implies that if $b_y+v_{\rm Ay}$ passes through zero, b_x must increase to compensate, even though if it decreased instead it could in principle help to form switchbacks. It is also worth mentioning that Eq. (17) remains valid even for radial $\boldsymbol{v}_{\rm A}$ or for $a\lesssim 1/\theta_{\perp 0}$, when $b_\parallel$ is instead dominated by the contribution from $b_x\hat{v}_{{\rm A}x}$; but, in this regime it does not provide any obviously useful constraint.

Also of interest is that Eq. (17) excludes the possibility that the field rotates beyond 90° in the $+\hat{\boldsymbol{y}}$ direction (i.e. the +T direction) at all. Such a rotation would involve $(b_y+v_{\rm Ay})^2$ reaching a maximum value then decreasing, while b_x would have to continuously decrease, which is impossible due to the monotonic dependence of b_x on $(b_y+v_{\rm Ay})^2$. Put together with the discussion of the previous paragraph, this provides an alternate way to consider the switchback skewness: a field rotation from $\hat{\boldsymbol{v}}_{\rm A}$ in the +T ($+\hat{\boldsymbol{y}}$ direction) is limited to be less than $90^\circ-\Phi$ when projected onto the x,y plane; but, a field rotation in the -T direction can rotate the field by $90^\circ+\Phi$. This leads to a strongly asymmetrical distribution of field rotations. This feature is clearly seen in the 3-D simulations of J+22 (see their figure 7-9), despite the fields therein obviously not satisfying the 1-D approximation used to derive Eq. (17).

B. Switchback sharpness, irregularity, and the direction of the mean field

The most obvious feature of the solutions shown in Fig. 4 is how sharp and irregular the switchbacks become, *viz.,* solutions feature wide quiet sections interpersed by sudden and rapid switchbacks as b_y changes sign. That these solutions evolve to become significantly sharper and more sporadic than those with radial $\boldsymbol{v}_{\rm A}$ is clear from a quick by-eye comparison with Fig. 5, which shows wave evolution in a radial mean field with the same initial b_n. We also show in Fig. 6 the "steepening factor" $Q\equiv\overline{|\partial_\lambda \boldsymbol{b}|^2}/\overline{|\boldsymbol{b}|^2}$ (M+21), for the same set of 1-D waves as shown in Fig. 3, which demonstrates the same idea more quantitatively and shows how the effect is even stronger for larger Φ. Promisingly, we see evidence that this effect of the Parker spiral enhancing switchback sharpness carries over to fully 3-D solutions (see figure 5 of J+22), which suggests it may be observable in the solar wind.

To understand why the effect occurs, we must simply couple the fact that $\overline{b_y}=0$ to the conclusion of the previous paragraph that ±T field rotations are limited to angles

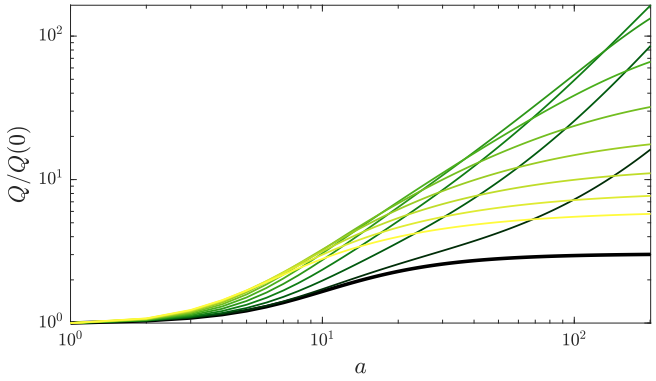

FIG. 6. Waveform sharpness, as measured by "steepening factor" $Q\equiv\overline{|\partial_\lambda \boldsymbol{b}|^2}/\overline{|\boldsymbol{b}|^2}$ for the same set of waves as shown in Fig. 3 (evolved using Eqs. (7) and (8)). The color scheme is the same, with the thick black line showing the radial-$\boldsymbol{v}_{\rm A}$ case and the colors showing increasing Φ_0 in steps of 2° from dark green to yellow. In a radial mean field, there is very little generation of sharp structures, as is clear from Fig. 5. The Parker spiral significantly changes this, causing the development of much sharper waves even after relatively short evolution times (see Fig. 4).

$<90^\circ\mp\Phi$ from the mean field (projected onto the radial-tangential plane). As the Parker spiral rotates further, the difference between these two directions increases further, but $\overline{b_y}$ remains zero, implying that the field must spend more volume rotated in the +T direction than the -T direction to compensate for the limited size of the +T rotations. The consequence is clearly seen in the bottom half of Fig. 4 (for $a\gtrsim 15$ or so, once Φ becomes significant): the solutions spend wide regions with modest $b_y>0$, then suddenly rotate to $b_y<0$ over short distances. This leads to both sharper waveforms and a more irregular, intermittent distribution of $b_\parallel$ fluctuations.

A corollary of the previous paragraph's discussion relates to measuring the Parker spiral direction. In particular, the mode of the field-direction (its most-common direction) becomes quite different to the mean-field direction $\hat{\boldsymbol{v}}_{\rm A}$, which is the direction in which the waves actually propagate. This is particularly clear from e.g., the $a=30$ panel in Fig. 4, which has $\Phi\approx 45^\circ$, but, discounting the switchbacks, one would conclude $3v_{{\rm A}x}\approx v_{\rm Ay}$, or an angle of $\approx 70^\circ$. This feature is also clearly seen in the simulations of J+22 (see their figure 7), suggesting that in measuring the Parker spiral angle in the solar wind, one must be careful to resolve the distinction between statistical mean and mode.

Finally, we note that the comparison between Figs. 3, 4 and 6 reveals an interesting consequence of the intermittent switchback rotations. Once Φ rotates beyond 45° and A starts decreasing, fluctuations in $b_\parallel/v_{\rm A}$ also decrease, if measured by their root mean square deviation (see Fig. 3, which matches the prediction Eq. (5)). However, we see from Fig. 4 that this decrease does not involve individual switchbacks becoming smaller, but rather a decrease in their volume-filling fraction. This is clear from the fact that the relative size of individual $b_\parallel/v_{\rm A}$ fluctuations increases from $a=50$ to $a=200$ in Fig. 4,

and that Q (the waveform steepness) continues to grow rapidly at large a (Fig. 6). This trend appears to continue up until arbitrarily large a for waves with $\theta_{\perp 0} \gg \Phi_0$, with nominally small-$A$ solutions containing extreme and sudden changes in field direction. Nonetheless, although interesting, we do not expect this property to be particularly important to the solar wind: by such large a with $\Phi \gtrsim 45^\circ$, there has likely been significant reflection of forward into backwards propagating waves and turbulence, which in general seems to destroy the constant-B requirement needed to form such solutions (see § V B below and figure 3b of J+22).

V. DISCUSSION: HEURISTIC APPLICATION TO 3-D FIELDS

In this section, we provide some commentary on how our results can be applied to fully 3-D fields, as needed for application to the solar wind. We also, in App. A, provide a different — more generic but less informative — argument for the results from § III B that switchbacks are enhanced by the Parker spiral and form preferentially with field rotations that lie in its plane ($\hat{\boldsymbol{p}}^{(\mathrm{Z})}$ in the out-of-plane direction). A key idea in this argument, as well as for the qualitative discussion, is that expansion generically tends to expand structures in the perpendicular plane (i.e., make them pancake shaped), or equivalently, to rotate the wave vectors to become more radial. In the presence of turbulence — which, to the contrary, tends to elongate structures along the background magnetic field — the competition with expansion will presumably enhance the power in radially aligned (as opposed to field perpendicular) wavevectors, compared to turbulence without expansion. Indeed, this seems to be observed in EBM simulations [33], and likely also in the solar wind [34, 35].

In order to appraise the application to 3-D fields in more detail, let us start by pointing out that there are (at least) three important differences in 3-D that are lacking from the 1-D results above. The first and most obvious is structure: simply the fact that fields vary in all three directions, not just in $\boldsymbol{p}$. The second is reflection-driven turbulence, which cannot affect 1-D fields because the nonlinear term vanishes (indeed it is this feature that enables the derivation of Eq. (7); M+21), but will in general cause the destruction of the pure Alfvénic state, the decay of fields compared to the WKB expectations, and the (re-)population of power across a wide range of wavenumbers. The third is parametric decay [36–38] — i.e., instability of the nonlinear Alfvénic solutions — which can destroy the wave if its perturbations grow sufficiently large. While this can occur in 1-D also, it is convenient to discuss it here because it is not captured by our analysis or by Eqs. (7) and (8). Let us address each of these in turn.

A. Structure

Realistic solar-wind fields presumably involve power across a wide range of wavenumber directions, distributed in such a way as to ensure constant B^2. We suggest that because the key physical ingredients needed for most of our results above are relatively simple — $\nabla \cdot \boldsymbol{b} = 0$, $B^2 = \text{const.}$, and the driving of $\boldsymbol{p}$ towards the radial direction — these results can also apply in 3-D with important caveats. In this application, the $\boldsymbol{p}$ direction should correspond to the direction of fastest variation across some particular substructure of the 3-D field. The simplest example of this viewpoint is from Eq. (5), which shows that near-perpendicular wavenumbers generate large $b_\parallel$ perturbations because of the the constant-B constraint. As discussed in M+21, the application to 3-D fields is straightforward, implying that structures that vary rapidly in the nearly perpendicular direction — in other words, those that are elongated along the mean magnetic field — drive larger $b_\parallel$. This feature has been seen in both simulations [39] and observations [27].

A similar application is to the conclusions of § III B, that a Parker spiral should enhance switchback formation, and that switchback field deflections occur preferentially in the tangential plane. As demonstrated in more detail in App. A, when structures are compressed to perpendicular pancakes by expansion ($p_x \gtrsim p_y, p_z$ on average), wavenumbers are on average more perpendicular to a mean field with a Parker spiral than a radial mean field, causing enhanced switchback occurrence rates by Eq. (5). Similarly, if $\boldsymbol{v}_\mathrm{A}$ involves a Parker spiral and the wavenumber distribution is biased towards the radial direction, wavenumbers that lie perpendicular to the plane of Parker spiral ($\hat{\boldsymbol{p}}^{(\mathrm{Z})}$ waves) are on average more perpendicular to $\boldsymbol{v}_\mathrm{A}$ than those in the plane of the Parker spiral. Even in 3-D, Alfvénically polarized fluctuations involve larger field perturbations perpendicular to their direction of fastest variation, implying that the structures that generate larger switchbacks are more likely to involve tangential rotations of $\boldsymbol{b}$ in the plane of the Parker spiral (i.e., b_y). Indeed, both of these features are seen in the simulations of J+22, with their figure 6 showing the stronger switchback growth with a Parker spiral, and their figures 7-9 showing various measures of deflections becoming tangentially asymmetric. Tangential asymmetry of deflections is also seen quite clearly in PSP data [18]. Nonetheless, turbulence provides an important caveat, particularly to the conclusion about switchback growth (see below).

More complex are the conclusions of § IV, where we showed that waves become strongly tangentially skewed. As well as $\nabla \cdot \boldsymbol{b} = 0$ and constant B^2, this conclusion relies on the idea that the $b_\parallel$ of a switchback becomes dominated by the b_y contribution, rather than the radial (b_x) fluctuation. This in turn relied on the wavevector becoming predominantly radial as $\boldsymbol{v}_\mathrm{A}$ rotates away from the radial (see Eq. (15)). If these conditions are satisfied, Eq. (17) suggests that structures that vary fastest in the near-radial direction ($\theta_p \lesssim 45^\circ$), but nonetheless remain somewhat perpendicular to $\boldsymbol{v}_\mathrm{A}$ ($\vartheta \gtrsim 45^\circ$), must increase their radial-field perturbation through a switchback in order to maintain constant B. This makes them tangentially skewed, therefore causing a significant difference between the statistical mean and mode of the magnetic-field direction. This condition — that quasi-radial $\theta_p \lesssim 45^\circ$ structures start dominating switchbacks for modest $\Phi \lesssim 45^\circ$ — does not seem unreasonable, so long as the turbulence is not continually repopulating modes along $\boldsymbol{v}_\mathrm{A}$ as fast as they are being ro-

tated radially by expansion (see below). Indeed, such tangential skewness is undeniably obvious in the Parker spiral simulation of J+22 (see their figures 7c and 8), which provides at least a basic confirmation of the above scenario. The feature is less clear in a recent analysis of PSP deflections [18], although it seems to be present in some cases (most prominently, encounter E6) and will be influenced by the Parker spiral angle, the fluctuation's amplitude, and the analysis method (e.g., the deflection angles that are counted as switchbacks). The enhanced switchback sharpness (§ IV B) seems to result from $\sin\vartheta$ being an increasing function of time, so presumably applies under similar circumstances with similar caveats. This feature is also observed in figure 5 of J+22, with the Parker spiral simulation exhibiting more sharp field rotations.

B. Turbulence

Turbulence in the solar wind is thought to be caused by (among other possibilities) the reflection of outwards- to inwards-propagating perturbations [40], whose amplitudes we will term z^+ and z^-, respectively. If this happens sufficiently rapidly so as to to cause the ratio z^-/z^+ (the imbalance) to grow continuously, the process will destroy the nonlinear solution Eq. (1), eventually breaking the constant-B condition and invalidating all of our arguments above. Indeed, the start of this process can be observed at late times in most simulations of J+22, with $C_{\boldsymbol{B}^2}$ (a measure of the relative spherical polarization) increasing at late times as the imbalance decreases (see their figures 2b & 3b). In the solar wind, such a process is at least only partially complete by $\sim$1AU, where turbulence is still observed to be relatively imbalanced and spherically polarized [41]; nonetheless, all of our results for $\Phi \gtrsim 45^\circ$ (e.g., the bottom two panels of Fig. 4) are clearly suspect and will likely be invalidated by this effect. However, even well before $z^- \sim z^+$, turbulence causes two other effects that invalidate our arguments if they are sufficiently strong: the first is the turbulent decay of the magnetic field; the second is the re-population of wavenumbers through nonlinear interactions. Turbulent decay will decrease the growth of wave amplitude below $A \propto a^{1/2}$, as used in our estimates (for $\Phi \ll 45^\circ$); clearly if waves stop growing there will likewise be no growth of switchbacks (unless perhaps if $A \gtrsim 1$ already and $\sin\vartheta$ increases). Similarly, if the interaction between different modes $\boldsymbol{p}$ is stronger than the effect of expansion, the scaling of $\boldsymbol{p}$ used in the arguments above will be incorrect (although there will presumably be some expansion-driven bias towards the radial direction). While this does not necessarily hinder switchback formation — indeed, stopping the decrease in $\sin\vartheta$ would be helpful — it would at least invalidate our scalings.

J+22 argued (see their §IIC), based on previous work [42–44], that the importance of the effects discussed above should be determined by the parameter $\chi \approx k_\perp z^+/k_\parallel v_\mathrm{A} \approx A k_\perp/k_\parallel$, which is a measure of the relative size of nonlinear effects ($k_\perp z^+$) and wave propagation ($k_\parallel v_\mathrm{A}$) for the z^- waves (here $k_\perp$ and $k_\parallel$ should be interpreted as average inverse correlation lengths of the energetically dominant z^+ structures, which source z^- through reflection). For $\chi \gtrsim 1$, the phenomenology suggests turbulent decay balances expansion-induced growth such that $A \propto a^0$ and waves do not grow at all (this is tentatively supported by the results of a $\chi > 1$ simulation in J+22; see their figure 2a). In this case, our results likely do not apply. In contrast, for $\chi \lesssim 1$, turbulent effects are weaker, and many of our results for 1-D waves seem to apply relatively well to 3-D, as evidenced by the multiple items of agreement discussed above. This conclusion — that the applicability our results in 3-D is determined by χ — requires further study and is currently quite poorly understood. For instance, the phenomenology seems to predict faster decay than seen in simulations and observations [43–45], and kinetic effects could also play a dominant role if they halt turbulent decay [46].

Finally, it is worth reiterating that these conclusions about turbulence, and indeed all of our results, apply only to regions of super-Alfvénic wind beyond the Alfvén surface because they use the expanding box model. In the sub-Alfvénic wind, fluctuation amplitudes almost certainly grow robustly even in the presence of turbulence [47, 48], while without turbulence waves grow much more rapidly than Eq. (10). In addition, if we interpret a as the cross-sectional area of a flux tube (see J+22 §IID), the scaling of $\boldsymbol{p}$ and Φ with a is quite different in sub-Alfvénic regions [49, 50], and of course $\Phi \ll 1$ in such regions anyway. Thus, for all our results, it is imagined that fluctuations have arrived already with a relatively large amplitude, and perhaps switchbacks, at the Alfvén point. It does not seem possible to grow large switchbacks from very small amplitude fluctuations in the EBM because of the turbulent decay (see §IIC of J+22).

C. Parametric decay

A third physical aspect that is missed out by our analysis is parametric decay, *viz.,* instability of the nonlinear Alfvénic solution (1) [38]. This can afflict even 1-D waves, however it is not captured by the reduced equations (7)–(8) on which we base our analysis. In general, it can cause break up of the wave if the instability grows to saturate at large amplitudes. Its growth rate, which will determine the time before saturation, generally increases with wave amplitude and at lower plasma β. For both general parallel fluctuations [51] and oblique large-amplitude waves of the form discussed in § II B [52], parametric instability has been found to be quite virulent, leading to saturation with $z^+ \sim z^-$. However, Ref. 53 found that expansion strongly decreased the growth rate of the instability in the EBM, which is likely due to the dynamics slowing down as the plasma expands, suggesting waves with frequencies ω_A not too far above $\dot{a}/a$ could propagate undisrupted over a relatively wide range of a (in contrast Ref. 54 find parallel waves are rapidly destroyed in the inner heliosphere, so more work is needed to better understand the influence of expansion). Perhaps more importantly, there are hints that the instability saturates at much lower levels in 2-D or 3-D fields [29, 55], maintaining the nonlinear Alfvénic state (1) nearly unchanged with $z^- \ll z^+$ even after saturation (although the instability may still play a key role in seeding turbulence [39]).

In addition, parametric decay is at least partially stabilized by damping of compressive fluctuations (which should be strong in a collisionless plasma), and random structure in the background Alfvénic state [37]. Overall, more study is needed to better understand the relevance of parametric instability compared to reflection-driven turbulence, but if it either grows too slowly or saturates at low levels, it will not significantly change our results.

VI. CONCLUSIONS

In this paper, we have explored the influence of the Parker spiral on the evolution of Alfvénic switchbacks in an expanding plasma. Using simple, geometric arguments based on spherically polarized 1-D waves, we find a surprisingly large effect. This highlights the interesting, nonintuitive physics of nonlinear Alfvénic perturbations, underscoring that particular care must be taken before attributing any observed asymmetrical (or otherwise unexpected) characteristics of switchbacks to properties of their source. The key differences compared to the case with a radial mean field all result from the nontrivial (non-monotonic) evolution of the wave's obliquity $\sin\vartheta$, which is brought by the simultaneous rotation of the mean field $\boldsymbol{v}_\mathrm{A}$ and mode wavevector $\boldsymbol{p}$ in different directions. Surprisingly, despite the normalised amplitude of waves in a Parker spiral growing more slowly than with a radial mean field, the formation of switchbacks is strongly enhanced in the most relevant regimes (c.f. black and green lines in Fig. 2). This conclusion may be testable in the solar wind by comparing streams with different mean-field directions but similar fluctuation amplitudes. Our other main conclusions are as follows:

(i) Switchbacks preferentially involve field rotations in the tangential direction, *viz.,* a rotation in the plane of the Parker spiral. This is because wavevectors perpendicular to the plane of the Parker spiral ($\hat{\boldsymbol{p}}^{(\mathrm{Z})}$ or $\cos\varphi = 0$) are more effective at generating parallel field perturbations than those in the plane of the Parker spiral ($\hat{\boldsymbol{p}}^{(\mathrm{Y})}$ or $\cos\varphi = \pm 1$). This conclusion is based on both the evolution of 1-D waves (§ III B) and a simple argument based on the average obliquity of wavevectors in a spectrum biased by radial expansion (App. A).

(ii) Tangential switchbacks (those discussed in conclusion (i)) become strongly "tangentially skewed," meaning the sharp field rotations of the switchback preferentially occur in one direction (towards the radial component of the mean field). This is a consequence of the divergence-free constraint in a spherically polarized wave, which forces the radial-field fluctuation to increase, rather than decrease, as the tangential field passes through zero (§ IV A). A similar constraint is that, projected on to the radial-tangential plane, field rotations in the $\pm$T direction are limited to angles $\leq 90^\circ \mp \Phi$, where Φ is the Parker-spiral angle; thus $-$T field rotations can be significantly larger, causing a highly asymmetrical rotation distribution.

(iii) As a consequence of conclusion (ii), and in order to maintain mean-zero fluctuations, the field-direction mode (its most common direction) is strongly skewed towards the $+$T direction compared to the mean field, *viz.,* it usually rotated to a larger angle than Φ. This suggests that care must be taken in measuring the Parker spiral, which should be the mean-field direction (that being the direction in which Alfvénic perturbations propagate).

(iv) As another consequence of conclusions (ii) and (iii), switchback fluctuations in a Parker spiral become more intermittent and sharper than those in a radial mean field. There are long quiet periods in which the field is rotated beyond Φ, interspersed with short and sudden large rotations (see Fig. 4).

Although these conclusions are clearly limited by our reliance on 1-D wave physics, we provide an extended commentary in § V about the general applicability to 3-D fields with turbulence. This suggests that there can be significant caveats, sometimes to the point of nullifying most of our results (e.g., in regimes where turbulence nonlinearities completely dominate over expansion), but also regimes where we might expect our results to apply qualitatively, even in 3-D. More importantly, in our companion paper J+22, we see evidence for all five of the above conclusions (enhanced switchbacks in the Parker spiral, plus each of points (i)–(iv) above) in full 3-D compressible expanding-box MHD simulations. Conclusions (ii)–(iii), on the skewness of tangential switchbacks, are particularly clear in field-deflection distributions (see figures 7-9 of J+22). There may also be tentative evidence for observations of these features in PSP and other spacecraft data: Refs. 18 and 26 see enhanced numbers of switchbacks with tangential deflections per point (i) above; Ref. 10 reports that switchbacks preferentially deflect to one side as per point (ii) above (the feature is less clear, though plausibly present, in the analysis of Ref. 18). The other predictions are also potentially observable — for instance, one could compare switchbacks between streams with different Parker spiral angles to investigate point (iv) or the overall prevalence of switchbacks — but require further work.

ACKNOWLEDGMENTS

The authors thank R. Laker, T. Horbury, and S. Bale for interesting discussions in the course of this work. Support for J.S. was provided by Rutherford Discovery Fellowship RDF-U001804, which is managed through the Royal Society Te Apārangi. Z.J. was supported by a postgraduate scholarship publishing bursary from the University of Otago. A.M. acknowledges the support of NASA through grant 80NSSC21K0462. R.M. was supported by Marsden fund grant MFP-U0020, managed through the Royal Society Te Apārangi.

Appendix A: Preferential tangential deflections in 3-D fields due to expansion

In this appendix, we provide an alternate argument for two of the main results of § III: (i) that the Parker spiral tends to enhance switchback formation, and (ii) that switchbacks in a Parker spiral tend to involve tangential, rather than normal,

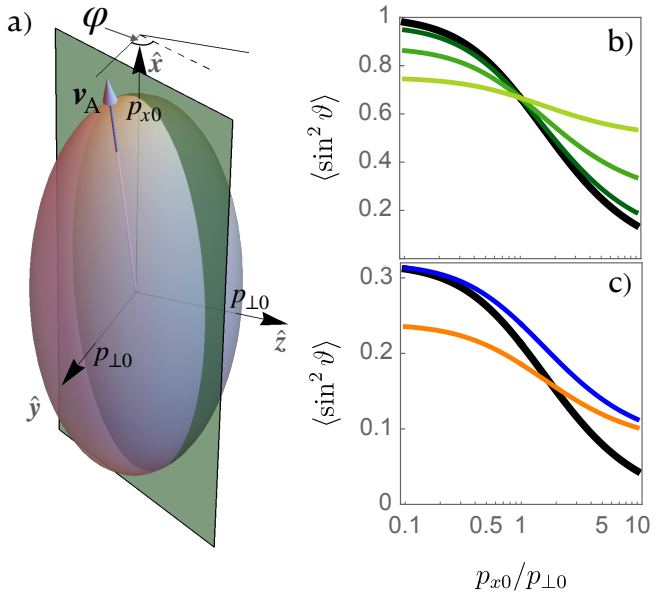

FIG. 7. Estimates of the switchback prevalence occurring due to a Gaussian spectrum of waves that is misaligned with the $\hat{\boldsymbol{v}}_A$ direction. Panel a) shows the geometry, with a representative contour of the spectrum Eq. (A1) along with the mean field and the plane slice at angle φ, which is used to estimate the contribution from different deflection directions. Panel b) shows the integral (A2), which estimates the average $\sin^2\vartheta$ of the spectrum as a function of $\xi_p = p_{x0}/p_{\perp 0}$ for a radial $\boldsymbol{v}_A$ (black curve) and $\Phi = 15^\circ, 30^\circ$, and 45° shown from dark green to light green. Panel c) shows the contribution to the integral (A2) from fluctuations in the plane of the Parker spiral ($\varphi = 0$ or π; orange line) or perpendicular to this plane ($\varphi = \pm\pi/2$; blue line), demonstrating that tangential field deflections will cause larger switchbacks. The black line shows $\Phi = 0$ for comparison.

deflections. Our method is simply to posit a simple Gaussian form for a spectrum of waves with its axis aligned along the radial direction, then compute the average $\sin^2\vartheta$ formed by such a spectrum when the mean field lies at angle Φ to the radial. In reality, of course, the spectrum should be neither Gaussian nor aligned perfectly along the radial: its alignment will presumably result from a competition between the expansion, which would tend to create spectral contours that are elongated along the radial direction, and turbulence, which tends to create spectral contours that are pancake shaped about the mean field. Nonetheless, the argument is relatively simple, does not have strong dependence on the chosen functional form of the spectrum, and can be trivially extended to account for nonradial alignment of the spectrum by simply redefining Φ as the angle between $\boldsymbol{v}_A$ and the spectrum's axis of symmetry (if this exists).

With this idea in mind, the assumed geometry is shown in Fig. 7a. We take the Gaussian spectrum,

$$E(p_x, p_\perp) = \frac{E_0}{\pi^{3/2} p_{x0} p_{\perp 0}^2} \exp\left(-\frac{p_\perp^2}{p_{\perp 0}^2} - \frac{p_x^2}{p_{x0}^2}\right), \qquad \text{(A1)}$$

where $p_\perp^2 = p_y^2 + p_z^2$ implies we assume symmetry about the radial (x) axis. As in the main text, we take $\boldsymbol{v}_A = v_A(\cos\Phi, \sin\Phi, 0)$, where Φ is the Parker spiral angle. The spectral properties are then specified by the anisotropy $\xi_p \equiv p_{x0}/p_{\perp 0}$, with $\xi_p > 1$ implying that outer-scale eddies are perpendicularly extended pancakes (elongated in p_x), and $\xi_p < 1$ implying the opposite [56]. Equation (5) says that for large-amplitude ($A \gtrsim \sin\vartheta$) waves, a measure of the switchback prevalence is $(b_\parallel/v_A)^2 \sim A^2 \sin^2\vartheta$. Equating $E(p_x, p_\perp)$ with A^2 of a given mode at $p_x, p_\perp$, we see that the relative switchback prevalence for a given amplitude, in the large amplitude regime of Eq. (5), is $(b_\parallel^2/v_A^2)/A^2 \sim \langle \sin^2\vartheta \rangle = E_0^{-1} \int d\boldsymbol{p} E(p_x, p_\perp) \sin^2\vartheta$. We can evaluate this integral using $\sin^2\vartheta = 1 - (\boldsymbol{p}\cdot\hat{\boldsymbol{v}}_A)^2/p^2$ by writing $p_y = p_\perp \cos\varphi$, $p_z = p_\perp \sin\varphi$ and integrating over $p_\perp$ and p_x. This gives

$$\langle \sin^2\vartheta \rangle = \int_0^{2\pi} d\varphi \left\{ \frac{\xi_p^2}{2\pi \tilde{\xi}_p^3} (\cos^2\Phi - \cos^2\varphi \sin^2\Phi) \tan^{-1}\tilde{\xi}_p - \frac{1}{2\pi\tilde{\xi}_p^2} [\sin^2\Phi(\xi_p^2 - 1 + \cos^2\varphi) - \cos^2\Phi] \right\}, \qquad \text{(A2)}$$

where $\tilde{\xi}_p^2 = \xi_p^2 - 1$ and (despite appearances) the expression is valid for both $\xi_p > 1$ and $\xi_p < 1$ (the $\tan^{-1}\tilde{\xi}_p$ becomes $i\tanh^{-1}|\tilde{\xi}_p|$ for $\xi_p < 1$).

If we first consider carrying out the φ integral in Eq. (A2), this allows the comparison of the total relative prevalence of switchbacks at different Φ. The result is plotted in Fig. 7b as a function of $\xi_p = p_{x0}/p_{\perp 0}$. As expected and intuitive from the geometry, for $\xi_p > 1$ the Parker spiral (green to yellow curves) increases $\langle \sin^2\vartheta \rangle$, while the opposite occurs for $\xi_p < 1$. This demonstrates that if eddies become expanded into perpendicular pancake structures by expansion, the Parker spiral increases the average obliquity of the spectrum thus enhancing switchbacks for the same amplitude. This is effectively the same physics as discussed in § III B, which showed that nonzero Φ increases $b_\parallel/v_A$ significantly for $a \gtrsim a_{\vartheta_{\min}}$, which can only occur once $\theta_p > 45^\circ$ in the relevant regime.

The second conclusion from § III B was that switchback deflections should be primarily tangential (in b_y), because many of the wavevectors in the Parker-spiral plane (which create normal field deflections) become highly parallel (Fig. 2b). To assess this conclusion for the spectrum (A1), we imagine considering the contribution of each φ in Eq. (A2) separately. Wavevectors with $\varphi = 0$ or π will cause larger b_z perturbations (because an Alfvénic perturbation has polarization $\sim\hat{\boldsymbol{p}} \times \boldsymbol{v}_A$), while those with $\varphi = \pm\pi/2$ will cause large b_y perturbations. We plot twice the integrand of Eq. (A2) in Fig. 7c, which captures the contribution to $\langle \sin^2\vartheta \rangle$ from the p-space plane angled at φ, as illustrated in Fig. 7a (this normalization is such that π multiplied by the black $\Phi = 0$ curve in Fig. 7c yields the same curve in Fig. 7b). We see that when $\Phi = 30^\circ$ the contribution from $\varphi = 0$ or π (orange curve) is quite small compared to that from $\varphi = \pm\pi/2$ (blue curves), for any value of χ_p. This is not surprising, and is indeed rather obvious by inspection of Fig. 7a; but, it demonstrates mathematically that in a random collection of waves with a random series of Alfvénic deflections, field deflections in the tangential direction (those with

$|\varphi| \approx \pi/2$) will cause larger parallel-field perturbations than deflections in the normal direction.

Appendix B: Comparison to MHD solutions

In this appendix we directly compare the predictions of Eqs. (7) and (8), which has been used in the main text to understand nonlinear wave evolution, to nonlinear isothermal expanding-box MHD simulations with the `Athena++` code. The purpose of this comparison is two fold. First, it is simply interesting to better understand the accuracy and applicability of Eqs. (7) and (8), given it was derived through an asymptotic expansion in a slow expansion rate. On this aspect, the comparison is extremely positive. Second, we noted in § IV that when $\boldsymbol{p}$ and $\boldsymbol{v}_\mathrm{A}$ lie in the same plane (the $\hat{\boldsymbol{p}}^{(\mathrm{Y})}$ case with $\varphi = 0$ or π), Eqs. (7) and (8) usually fail to produce solutions with constant B. Importantly, because Eqs. (7) and (8) are derived by assuming that $\boldsymbol{b}$ maintains constant B, if it does not, we cannot trust their results. It is thus interesting to see whether this production of non-constant B is truly physical — i.e., whether it also occurs in true MHD evolution — or whether it results for another reason related to the approximations used to derive Eqs. (7) and (8). Although the detailed cause of this behavior remains unclear, we speculate that it relates to $\sin\vartheta$ changing particularly rapidly in this geometry, with the shape of $\boldsymbol{b}$ not able to adjust fast enough to maintain constant B.

To generate the MHD solutions, we use the MHD code `Athena++`, with the modifications to capture plasma expansion detailed in J+22. We set up each wave in a 2-D domain of dimensions $L_x = 4L_y$ at $a = 1$, by initialising the sinusoidal $p_x = 2\pi/L_x$, $p_y = 2\pi/L_y$ mode in b_n (the component out of the plane) with amplitude 1, such that the wave obliquity is $\theta_{p0} = \tan^{-1}(L_x/L_y) \approx 76^\circ$. The other $\boldsymbol{b}$ components are constructed as described in Eq. (6) to ensure constant B, with an initial Parker spiral angle of 5° (if this is included). We choose the expansion rate to be $\dot{a}/a = 0.5\omega_\mathrm{A}$ (i.e., $\varepsilon = 0.5$) and use 128 grid points in each direction. In order to compare the solutions to Eq. (7), we perform a "wavefront average" at each output step, meaning we rotate the coordinate system to align with the wave (accounting for the periodicity of the domain), then spatially average in the direction perpendicular to $\boldsymbol{p}$.

Results for radial $\boldsymbol{v}_\mathrm{A}$ and $\varphi = \pi/2$ — *viz.,* the situations in which Eqs. (7) and (8) successfully maintain constant B — are shown in Fig. 8. Left and right subpanels compare wavefront-averaged solutions to the MHD equations to those of Eq. (7) at the same a and other parameters. We see excellent agreement between the general shape of the waveforms, discounting the phase of the wave, which evolves in the MHD case but not in Eq. (7). The MHD solutions do involve small fluctuations that are not present in Eq. (7), which are most clearly observable in the field magnitude profile; these result in part from the small compressive components neglected in Eq. (7) (see M+21), and in part from the parametric instability (these fluctuations vary across the wavefront direction so are averaged in Fig. 8). The parametric instability fluctuations slowly grow and eventually overwhelm the wave, but are not our primary interest here (see Ref. 53).

Results for $\varphi = 0$ and $\varphi = \pi$, when $\boldsymbol{p}$ and the Parker spiral lie in the same plane, are shown in Fig. 9. In these cases, we can clearly see in the right-hand subpanels that the solutions of Eqs. (7) and (8) do not maintain constant B, calling the validity of these solutions into question. Indeed, we see that B remains much more spatially constant in the MHD solutions, and the spatial form of the individual components differs more significantly than those shown in Fig. 8, although they clearly maintain similar structures. Particularly for the $\varphi = \pi$ case, we see tentative evidence that the MHD solutions exhibit larger variation in B than the cases in Fig. 8, suggesting that at least some of the failure of Eq. (7) to maintain constant B is physical. In the MHD solutions, these variations propagate around the box, steepening and reducing in size due to compressive processes that are not captured by Eqs. (7) and (8) (see, e.g., Ref. 57). While the situation in the $\varphi = 0$ solution is less clear, we clearly see smaller switchbacks in MHD in both cases, which presumably results from the combination of MHD more robustly maintaining a constant-B Alfvénic solution, and MHD dissipating or smoothing the wave energy that is converted into compressive structures. This latter effect would not be captured by the arguments in § III, suggesting that the $b_\parallel/v_\mathrm{A}$ estimated therein could be an overestimate. Also of note is that we do not see any obvious singular behavior (e.g., mode conversion) when $\sin\vartheta$ passes through zero in the $\varphi = 0$ case (around $a \approx 6$, as seen by the nearly flat $b_\parallel$ at this time).

Overall, we see tentative evidence that $\hat{\boldsymbol{p}}^{(\mathrm{Y})}$ waves have a tendency to generate larger compressive variations than $\hat{\boldsymbol{p}}^{(\mathrm{Z})}$ waves. This could enable other dissipation mechanisms in a real plasma thereby reducing the switchbacks generated by such waves. Thus, this strengthens our conclusions from § III, implying that, as well as naturally generating smaller $b_\parallel$ due to geometry, switchbacks that involve field rotations in the normal direction also are likely to dissipate more strongly, thus enhancing the dominance of tangential switchbacks.

Appendix C: The scaling of WKB waves in a strong Parker spiral

In deriving the scaling of wave amplitudes with expansion in the presence of a Parker spiral $v_{\mathrm{A}y} \sim v_{\mathrm{A}x}$, we used the same scaling of the wave amplitude with expansion, $\overline{|\boldsymbol{b}|} \propto a^{-1/2}$, as in the radial-background-field case. In this appendix, we confirm that this is indeed correct, *viz.,* that the scaling of the unnormalized amplitude of WKB Alfvén waves with a is independent of their direction of propagation. This property has been shown in a number of previous works for small amplitude waves [58, 59] and is also contained in the large-amplitude results of Refs. 21 and 31 and M+21 (the second term $(\dot{a}/2a)\boldsymbol{b}$ in Eq. (7) is independent of $\hat{\boldsymbol{v}}_\mathrm{A}$). Nonetheless, we feel that the EBM derivation below is helpful both for its generality (it does not assume 1-D waves or low amplitude) and its simplicity, which helps to illustrate the physical cause of the $\hat{\boldsymbol{v}}_\mathrm{A}$-independence of the amplitude scaling.

Starting from the EBM equations (see e.g., J+22), we as-

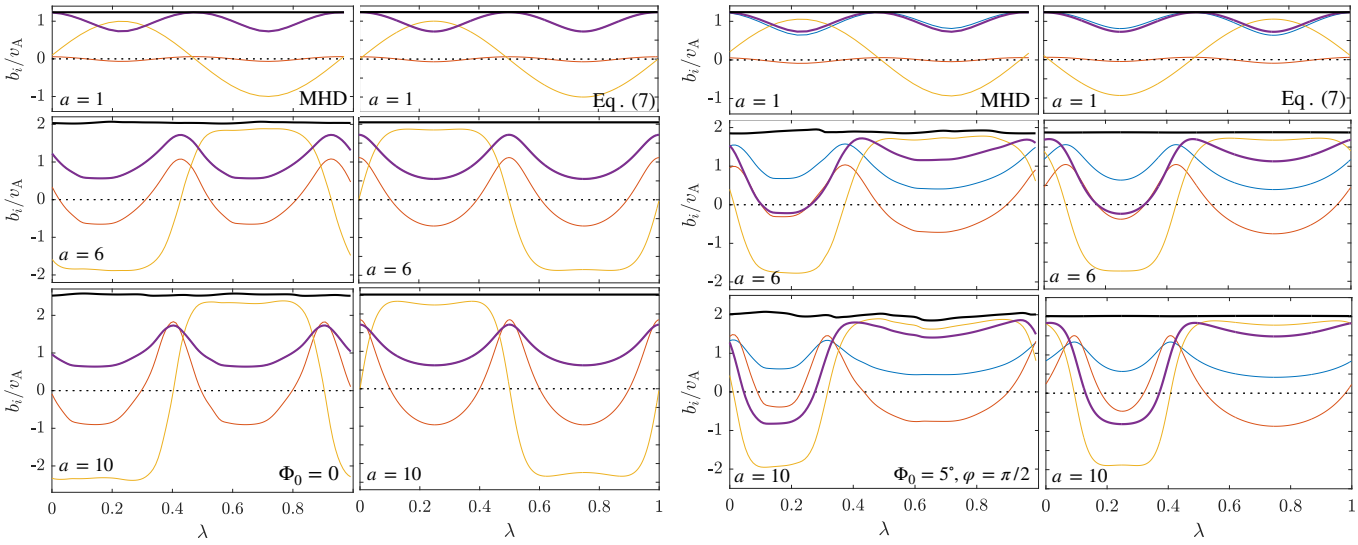

FIG. 8. Each panel shows the spatial form of an evolving 1-D wave, comparing the wavefront average of true expanding MHD solutions from 2-D simulations (left subpanels; see text) to solutions of Eqs. (7) and (8) (right subpanels). In each case, we start from a sinusoidal b_n perturbation, $b_n = \sin(2\pi\lambda)$ (giving $A \approx 1/\sqrt{2}$) with b_m computed to ensure constant B according to Eq. (6). The initial wave obliquity is $\theta_{p0} = \tan^{-1}(1/4) \approx 76°$, and in the MHD simulations we take $\varepsilon = (\dot{a}/a)/\omega_A = 0.5$. Line colors in each panel are the same as Fig. 4: thin blue, red, and yellow show $\hat{v}_{Ax} + b_x/v_A$, $\hat{v}_{Ay} + b_x/v_A$, and b_z/v_A, respectively, and the thick black and purple lines show the field magnitude $(B/\sqrt{4\pi\rho})/v_A$ and parallel perturbation $b_\parallel/v_A + 1$, respectively. The left-hand set of panels show the case of a radial $\boldsymbol{v}_A$, while the right-hand panels include a Parker spiral with $\Phi_0 = 5°$ and $\varphi = \pi/2$ (the case $\hat{\boldsymbol{p}}^{(Z)}$ in Fig. 1). We see that the agreement in the evolution, amplitude, and shape is excellent, and that the true MHD solutions have reasonably constant B despite the relatively large ε (there are some fluctuations in the MHD wave from the beginnings of parametric instability and compressive perturbations driven by expansion).

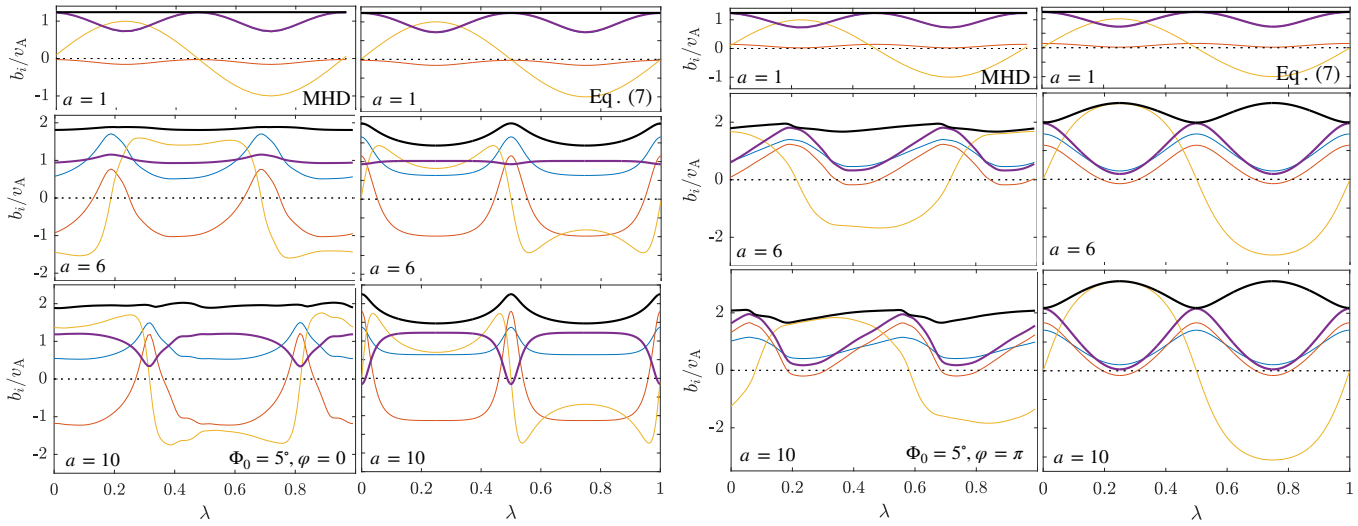

FIG. 9. As in Fig. 8, with the same initial conditions, θ_{p0}, and ε, but for the cases $\varphi = 0$ (left-hand panels) and $\varphi = \pi$ (right-hand panels), which both have $\hat{\boldsymbol{p}}$ and $\boldsymbol{v}_A$ lying in the same plane (case $\hat{\boldsymbol{p}}^{(Y)}$ in Fig. 1). In these cases, Eqs. (7) and (8) fail to produce constant-B solutions (see discussion in text), and the difference with the MHD solutions becomes more significant. In particular, the MHD solution much more effectively smooths the variation in B, generating comparatively smaller switchbacks in both cases.

sume constant ρ and incompressible motions, then form the equations for $\boldsymbol{z}^\pm = \boldsymbol{u} \pm \boldsymbol{B}/\sqrt{4\pi\rho} = \boldsymbol{u} \pm \boldsymbol{b} \pm \boldsymbol{v}_A$ (where, as above, $\boldsymbol{b}$ is $\delta\boldsymbol{B}/\sqrt{4\pi\rho}$). This gives

$$\partial_t \boldsymbol{z}^\pm \pm \boldsymbol{v}_A \cdot \tilde{\nabla} \boldsymbol{z}^\pm = -\tilde{\nabla}\tilde{p} + \boldsymbol{z}^\mp \cdot \tilde{\nabla} \boldsymbol{z}^\pm - \frac{\dot{a}}{2a}(z_x^\pm - z_x^\mp)\hat{\boldsymbol{x}} - \frac{\dot{a}}{2a}\mathsf{T} \cdot (\boldsymbol{z}^+ + \boldsymbol{z}^-), \quad \text{(C1)}$$

where $\mathsf{T} = \mathrm{diag}(0,1,1)$, $\tilde{\nabla}$ is the ∇ operator in the expanding frame, and $\tilde{p}$ is chosen to constrain $\tilde{\nabla}\cdot\boldsymbol{z}^{\pm} = 0$. The final two terms arise due to the differing influence of expansion on $\boldsymbol{b}$ (the second-to-last term) and $\boldsymbol{u}$ (the last term). To understand the scaling in the WKB limit neglecting nonlinear interactions, we can simply set $\boldsymbol{z}^{-}$ to zero. This is justified because when the $\boldsymbol{v}_{\rm A}\cdot\tilde{\nabla}$ term dominates the others, the reflection terms (those involving $\dot{a}/a\,\boldsymbol{z}^{+}$), cannot cause $\boldsymbol{z}^{-}$ grow because it quickly moves out of phase with the source $\boldsymbol{z}^{+}$ wave. Thus, in this limit, $(\partial_t + \boldsymbol{v}_{\rm A}\cdot\tilde{\nabla})\boldsymbol{z}^{+} \approx -(\dot{a}/2a)\boldsymbol{z}^{+}$ because both the third and forth terms on the right-hand-side of Eq. (C1) involve the same factor $-\dot{a}/2a$. This implies that $|\boldsymbol{z}^{+}|$ decays as $|\boldsymbol{z}^{+}| \propto a^{-1/2}$, no matter its direction or the direction of the mean field.

[1] S. D. Bale, S. T. Badman, J. W. Bonnell, T. A. Bowen, D. Burgess, et al., Nature **576**, 237 (2019).
[2] J. C. Kasper, S. D. Bale, J. W. Belcher, M. Berthomier, A. W. Case, B. D. G. Chandran, et al., Nature **576**, 228 (2019).
[3] S. D. Bale, T. S. Horbury, M. Velli, M. I. Desai, J. S. Halekas, M. D. McManus, O. Panasenco, S. T. Badman, T. A. Bowen, B. D. G. Chandran, et al., Astrophys. J. **923**, 174 (2021), 2109.01069.
[4] L. A. Fisk and J. C. Kasper, Astrophys. J. Lett. **894**, L4 (2020).
[5] J. F. Drake, O. Agapitov, M. Swisdak, S. T. Badman, S. D. Bale, T. S. Horbury, J. C. Kasper, R. J. MacDowall, F. S. Mozer, T. D. Phan, et al., Astron. Astro. **650**, A2 (2021), 2009.05645.
[6] G. P. Zank, M. Nakanotani, L. L. Zhao, L. Adhikari, and J. Kasper, Astrophys. J. **903**, 1 (2020).
[7] J. He, X. Zhu, L. Yang, C. Hou, D. Duan, L. Zhang, and Y. Wang, Astrophys. J. Lett. **913**, L14 (2021).
[8] A. C. Sterling and R. L. Moore, Astrophys. J. Lett. **896**, L18 (2020), 2006.04990.
[9] N. Magyar, D. Utz, R. Erdélyi, and V. M. Nakariakov, Astrophys. J. **911**, 75 (2021), 2103.03726.
[10] N. A. Schwadron and D. J. McComas, Astrophys. J. **909**, 95 (2021), 2102.03696.
[11] D. Ruffolo, W. H. Matthaeus, R. Chhiber, A. V. Usmanov, Y. Yang, R. Bandyopadhyay, T. N. Parashar, M. L. Goldstein, C. E. DeForest, M. Wan, et al., Astrophys. J. **902**, 94 (2020), 2009.06537.
[12] J. Squire, B. D. G. Chandran, and R. Meyrand, Astrophys. J. Lett. **891**, L2 (2020), 2001.08422.
[13] M. Shoda, B. D. G. Chandran, and S. R. Cranmer, Astrophys. J. **915**, 52 (2021), 2101.09529.
[14] A. Mallet, J. Squire, B. D. G. Chandran, T. Bowen, and S. D. Bale, Astrophys. J. **918**, 62 (2021).
[15] S. R. Cranmer, A. A. van Ballegooijen, and R. J. Edgar, Astrophys. J. Supp. **171**, 520 (2007), astro-ph/0703333.
[16] B. D. G. Chandran, J. Plasma Phys. **87**, 905870304 (2021), 2101.04156.
[17] B. De Pontieu, S. W. McIntosh, M. Carlsson, V. H. Hansteen, T. D. Tarbell, C. J. Schrijver, A. M. Title, R. A. Shine, S. Tsuneta, Y. Katsukawa, et al., Science **318**, 1574 (2007).
[18] R. Laker, T. S. Horbury, L. Matteini, S. D. Bale, J. E. Stawarz, L. D. Woodham, and T. Woolley, arXiv e-prints arXiv:2204.12980 (2022), 2204.12980.
[19] E. N. Parker, Astrophys. J. **128**, 664 (1958).
[20] Z. Johnston, J. Squire, A. Mallet, and R. Meyrand, On the properties of Alfvénic switchbacks in the expanding solar wind: three-dimensional numerical simulations, submitted (2022).
[21] A. Barnes and J. V. Hollweg, J. Geophys. Res. **79**, 2302 (1974).
[22] R. M. Kulsrud, in *Handbook of Plasma Physics*, edited by R. N. Sagdeev and M. N. Rosenbluth (Princeton University, 1983).
[23] P. B. Snyder, G. W. Hammett, and W. Dorland, Phys. Plasmas **4**, 3974 (1997).
[24] A. Barnes and G. C. J. Suffolk, J. Plasma Phys. **5**, 315 (1971).
[25] B. J. Vasquez and J. V. Hollweg, J. Geophys. Res.: Space Phys. **103**, 335 (1998).
[26] T. S. Horbury, T. Woolley, R. Laker, L. Matteini, J. Eastwood, S. D. Bale, M. Velli, B. D. G. Chandran, T. Phan, N. E. Raouafi, et al., Astrophys. J. Supp. **246**, 45 (2020).
[27] R. Laker, T. S. Horbury, S. D. Bale, L. Matteini, T. Woolley, L. D. Woodham, S. T. Badman, M. Pulupa, J. C. Kasper, M. Stevens, et al., Astron. Astro. **650**, A1 (2021), 2010.10211.
[28] D. A. Roberts, Phys. Rev. Lett. **109**, 231102 (2012).
[29] L. Primavera, F. Malara, S. Servidio, G. Nigro, and P. Veltri, Astrophys. J. **880**, 156 (2019).
[30] F. Valentini, F. Malara, L. Sorriso-Valvo, R. Bruno, and L. Primavera, Astrophys. J. Lett. **881**, L5 (2019).
[31] J. V. Hollweg, J. Geophys. Res. **79**, 1539 (1974).
[32] R. Grappin, M. Velli, and A. Mangeney, Phys. Rev. Lett. **70**, 2190 (1993).
[33] A. Verdini and R. Grappin, Astrophys. J. Lett. **808**, L34 (2015), 1506.03450.
[34] C. H. K. Chen, A. Mallet, A. A. Schekochihin, T. S. Horbury, R. T. Wicks, and S. D. Bale, Astrophys. J. **758**, 120 (2012), 1109.2558.
[35] A. Verdini, R. Grappin, O. Alexandrova, L. Franci, S. Landi, L. Matteini, and E. Papini, Mon. Not. R. Astron. Soc. **486**, 3006 (2019), 1904.04118.
[36] R. Z. Sagdeev and A. A. Galeev, *Nonlinear Plasma Theory* (New York: Benjamin, 1969).
[37] R. H. Cohen and R. L. Dewar, J. Geophys. Res. **79**, 4174 (1974).
[38] M. L. Goldstein, Astrophys. J. **219**, 700 (1978).
[39] M. Shoda, T. K. Suzuki, M. Asgari-Targhi, and T. Yokoyama, Astrophys. J. Lett. **880**, L2 (2019), 1905.11685.
[40] M. Velli, R. Grappin, and A. Mangeney, Phys. Rev. Lett. **63**, 1807 (1989).
[41] R. Bruno and V. Carbone, Living Rev. Solar Phys. **10**, 2 (2013).
[42] A. Verdini and M. Velli, Astrophys. J. **662**, 669 (2007), astro-ph/0702205.
[43] B. D. G. Chandran and J. V. Hollweg, Astrophys. J. **707**, 1659 (2009), 0911.1068.
[44] B. D. G. Chandran and J. C. Perez, J. Plasma Phys. **85**, 905850409 (2019), 1908.00880.
[45] A. A. van Ballegooijen and M. Asgari-Targhi, Astrophys. J. **821**, 106 (2016), 1602.06883.
[46] R. Meyrand, J. Squire, A. A. Schekochihin, and W. Dorland, J. Plasma Phys. **87**, 535870301 (2021), 2009.02828.
[47] A. A. van Ballegooijen, M. Asgari-Targhi, S. R. Cranmer, and E. E. DeLuca, Astrophys. J. **736**, 3 (2011), 1105.0402.
[48] J. C. Perez and B. D. G. Chandran, Astrophys. J. **776**, 124 (2013).
[49] E. J. Weber and J. Davis, Leverett, Astrophys. J. **148**, 217 (1967).
[50] A. Tenerani and M. Velli, Astrophys. J. **843**, 26 (2017),

1702.03014.
[51] F. Malara, L. Primavera, and P. Veltri, Phys. Plasmas **7**, 2866 (2000).
[52] L. Del Zanna, Geophys. Res. Lett. **28**, 2585 (2001).
[53] L. Del Zanna, L. Matteini, S. Landi, A. Verdini, and M. Velli, J. Plasma Phys. **81**, 325810102 (2015), 1407.5851.
[54] A. Tenerani and M. Velli, J. Geophys. Res.: Space Phys. **118**, 7507 (2013).
[55] A. Tenerani, M. Velli, L. Matteini, V. Réville, C. Shi, S. D. Bale, J. C. Kasper, J. W. Bonnell, A. W. Case, T. D. de Wit, et al., Astrophys. J. Supp. **246**, 32 (2020).
[56] One can generalize the argument by imagining that the competition between turbulence and expansion leads to a spectrum with its axis aligned between the radial and $\hat{\mathbf{v}}_{\rm A}$ directions. Then, our calculation follows in the same way with Φ redefined as the angle between the symmetry axis of the spectrum and the Parker spiral. However, the assumption of isotropy in $p_\perp$ is more questionable in this case, and one should really allow for differing p_z and p_y widths. Nonetheless, given we lack a good model of how this competition between turbulence and expansion manifests, while numerical integrations suggest that this does not make a significant difference to our qualitative conclusions anyway, it does not seem worthy of detailed exploration.
[57] R. H. Cohen and R. M. Kulsrud, Phys. Fluids **17**, 2215 (1974).
[58] Y. C. Whang, J. Geophys. Res. **78**, 7221 (1973).
[59] H. J. Völk and W. Aplers, Astrophys. Space Sci. **20**, 267 (1973).